Stem Cell Reports
Article
ISSCR
OPEN ACCESS

The Wnt-dependent master regulator NKX1-2 controls mouse pre-implantation development

Shoma Nakagawa,[1] Davide Carnevali,[1,14] Xiangtian Tan,[2,14] Mariano J. Alvarez,[2,3] David-Emlyn Parfitt,[4] Umberto Di Vicino,[1] Karthik Arumugam,[1] William Shin,[2] Sergi Aranda,[1] Davide Normanno,[1,5] Ruben Sebastian-Perez,[1] Chiara Cannatá,[1] Paola Cortes,[1] Maria Victoria Neguembor,[1] Michael M. Shen,[2,4] Andrea Califano,[2,6,7,8,9,13,*] and Maria Pia Cosma[1,10,11,12,15,*]

[1]Center for Genomic Regulation (CRG), The Barcelona Institute of Science and Technology, Dr. Aiguader 88, 08003 Barcelona, Spain
[2]Department of Systems Biology, Columbia University, New York, NY, USA
[3]DarwinHealth Inc, New York, NY, USA
[4]Departments of Medicine, Genetics and Development, Urology, and Systems Biology, Herbert Irving Comprehensive Cancer Center, Vagelos College of Physicians and Surgeons, Columbia University, New York, NY, USA
[5]Institute of Human Genetics, CNRS, Montpellier, France
[6]Herbert Irving Comprehensive Cancer Center, Columbia University, New York, NY, USA
[7]Department of Biochemistry and Molecular Biophysics, Vagelos College of Physicians and Surgeons, Columbia University, New York, NY, USA
[8]Department of Biomedical Informatics, Vagelos College of Physicians and Surgeons, Columbia University, New York, NY, USA
[9]Department of Medicine, Vagelos College of Physicians and Surgeons, Columbia University, New York, NY, USA
[10]ICREA, Pg.Lluis Companys 23, 08010 Barcelona, Spain
[11]Universitat Pompeu Fabra (UPF), Barcelona, Spain
[12]Medical Research Institute, Guangdong Provincial People's Hospital (Guangdong Academy of Medical Sciences), Southern Medical University, 106 Zhongshan Er Road, Yuexiu District, Guangzhou 510080, China
[13]Chan Zuckerberg Biohub New York, New York, NY, USA
[14]These authors contributed equally
[15]Lead contact
*Correspondence: ac2248@cumc.columbia.edu (A.C.), pia.cosma@crg.es (M.P.C.)
https://doi.org/10.1016/j.stemcr.2024.04.004

SUMMARY

Embryo size, specification, and homeostasis are regulated by a complex gene regulatory and signaling network. Here we used gene expression signatures of Wnt-activated mouse embryonic stem cell (mESC) clones to reverse engineer an mESC regulatory network. We identify NKX1-2 as a novel master regulator of preimplantation embryo development. We find that *Nkx1-2* inhibition reduces nascent RNA synthesis, downregulates genes controlling ribosome biogenesis, RNA translation, and transport, and induces severe alteration of nucleolus structure, resulting in the exclusion of RNA polymerase I from nucleoli. In turn, NKX1-2 loss of function leads to chromosome missegregation in the 2- to 4-cell embryo stages, severe decrease in blastomere numbers, alterations of tight junctions (TJs), and impairment of microlumen coarsening. Overall, these changes impair the blastocoel expansion-collapse cycle and embryo cavitation, leading to altered lineage specification and developmental arrest.

INTRODUCTION

Embryo formation begins in the one-cell zygote. After fertilization, the zygote reaches the blastocyst stage, consisting of an inner cell mass (ICM) and trophectoderm cells. The ICM is further differentiated into the epiblast (Epi) and the primitive endoderm (PrE) (Zhu and Zernicka-Goetz, 2020b). Precise cell fate specification during preimplantation development is essential for the subsequent post-implant and full-term development. Numerous consecutive events—such as the establishment of cellular polarity, embryo compaction, and symmetric and asymmetric cell division—govern lineage specification (White et al., 2016; Zhu and Zernicka-Goetz, 2020a).

The Wnt/β-catenin signaling cascade is highly conserved across the animal kingdom and is one of the most critical pathways controlling embryo development (Munoz-Descalzo et al., 2015; Xie et al., 2008). In mouse, it controls not only early development but also cell proliferation and tissue homeostasis (Aulicino et al., 2020). Following β-catenin knockout (KO), mouse embryos develop normally until 7 days after fertilization (embryonic day 7 [E7.0]) but are degraded at the gastrulation stage due to abnormal anterior-posterior body axis establishment (Haegel et al., 1995; Huelsken et al., 2000). Moreover, these embryos show disorganized mesodermal and endodermal germ cell layers (Kishimoto et al., 2020).

Several WNT proteins are expressed as early as in blastocyst embryos, predominantly in the ICM (Kemp et al., 2005). Notably, Wnt/β-catenin signaling pathway must be switched off upon implantation for proper development (ten Berge et al., 2008, 2011). While it is clear that the Wnt/β-catenin signaling pathway is important for post-implant development and mouse embryonic stem cell (mESC) establishment, it is not clear whether it also plays a key role in preimplantation development.

To address this question, we used an unbiased systems biology approach to elucidate the master regulator (MR)

proteins responsible for mechanistically implementing the transcriptional state of the cell (Alvarez et al., 2016). Specifically, we used the extensively validated VIPER (Virtual Inference of Protein-activity by Enriched Reglon analysis) algorithm (Alvarez et al., 2016; Obradovic et al., 2021; Paull et al., 2021) to transform the transcriptional profile of mutant mESC lines, expressing a constitutively active Wnt/β-catenin pathway or with a deletion of *Tcf3* (an inhibitor of the Wnt/β-catenin pathway) (Lluis et al., 2011; Merrill, 2012), into comprehensive protein activity profiles. This approach allowed us to identify regulatory factors that control the Wnt/β-catenin-mediated transcriptional state via their transcriptional targets. To generate the transcriptional targets of all regulatory proteins, we analyzed a large collection of mESC profiles using the ARACNe (Algorithm for the Reconstruction of Accurate Cellular Networks) algorithm (Basso et al., 2005). This analysis identified *Nkx1-2* (also known as *Sax-1*) as a novel Wnt/β-catenin effector and as an essential MR of preimplantation development in mouse embryos. In mice (and humans), NKX1-2 is a homeobox protein family member (Rovescalli et al., 2000). Inhibition of *Nkx1-2* resulted in i) mislocalization of RNA POLYMERASE I (POL I) from the nucleolus and the dysfunction of pathways and genes regulating ribosome biogenesis, RNA translation, and transport, resulting in chromosome missegregation, as early as the 2- to 4-cell stages, ii) loss of embryo cavitation, and iii) inappropriate lineage specification, culminating in embryo development arrest. Thus, we conclude that NKX1-2 controls nascent RNA synthesis, ribosomal biogenesis, and POL I localization in the nucleolus during preimplantation mouse embryo development.

RESULTS

Identification of Wnt/β-catenin pathway-dependent MRs that control pluripotency and preimplantation development

To identify yet-unknown Wnt pathway effectors that play a key role in controlling ESC pluripotency, we analyzed RNA sequencing (RNA-seq) profiles from i) wild-type (WT) mESCs, ii) two S33Y *β-catenin* mutant mESC clones (#1 and #2) (Theka et al., 2019), and iii) a *Tcf3* KO mESC line (Lluis et al., 2011). The Wnt pathway activity was higher in all three mutant mESCs than in WT mESCs, as measured using a Wnt reporter as previously reported (Theka et al., 2019), and Wnt activity was higher in clone #2 than in clone #1 (Theka et al., 2019). Principal-component analysis (PCA) showed that replicates of the clones #1 and #2, or of *Tcf3* KO mESCs, clustered together but that these clusters were separate from the corresponding WT mESCs (Figure 1A).

Analysis of differentially expressed genes (DEGs) in the mutant vs. WT cells showed that pluripotency regulators—including *Nanog*, *Pou5f1*, *Sox2*, *Esrrb*, and *Prdm14*, as well as the Wnt-dependent gene *Axin2*—were significantly upregulated in the *β-catenin* clones and in *Tcf3* KO mESCs (false discovery rate [FDR] <0.05), whereas lineage differentiation markers, such as *Fgf5*, *Dnmt3b*, *Krt18*, *T*, and *Neurog1*, were significantly downregulated (Figure 1B). Overall, we identified >4,000 DEGs (FDR <0.05) (Figure S1A), presenting a significant challenge to directly identifying potential mechanistic effectors of Wnt/β-catenin activation as candidate pluripotency drivers. To address this challenge, we used the VIPER algorithm, which is designed to identify proteins that mechanistically regulate a gene expression signature based on the differential expression of their transcriptional targets (Alvarez et al., 2016). We identified the context-specific transcriptional targets of all regulatory proteins (i.e., the mESC interactome) by analyzing a large collection of mESCs that had been perturbed with a combination of morphogens and small molecules, using the ARACNe algorithm (Basso et al., 2005; Lefebvre et al., 2010) (Tables S1 and S2). The statistical significance of the VIPER-measured differential protein activity in the mutant mESCs (both β-catenin mESC clones #1 and #2 and the *Tcf3* KO mESCs) vs. WT cells was generated by integrating *p* values across the six replicates of each condition, using Stouffer's method (Figure 1C).

Consistent with expectations, well-known pluripotency regulators (such as the transcription factors [TFs] NANOG [Nanog homeobox], PRMD14, and ESRRB) were identified in the top 30 candidate MR proteins inferred by the analysis (Figure 1C). Thus, we hypothesized that additional, uncharacterized pluripotency regulators could also be present in the most differentially active MRs. Specifically, we identified the TFs GLI2, NKX1-2, ZFP960, and DMBX1 as the four most differentially active proteins in Wnt-activated cells, suggesting their potential role as putative downstream Wnt pathway effectors, with a yet-to-be-defined role in pluripotency (Figure 1C). We then compared the VIPER activity of mESCs cultured with the Wnt inhibitor Dkk1 to that in WT cells. In Wnt-repressed mESCs, GLI2, ZFP960, and DMBX1 showed very low activity, while NKX1-2 showed no activity, suggesting that these factors are Wnt-dependent MRs (Figure S1B).

As the Wnt pathway is active in the ICM in preimplantation embryos (ten Berge et al., 2011), we next assessed the differential activity of the most statistically significant VIPER-inferred TFs in the ICM, using VIPER analysis of a published RNA-seq dataset from embryos at different preimplantation stages (Boroviak et al., 2015). The analysis confirmed the differential activity of TFs that are known lineage-specific markers of embryogenesis, as predicted by VIPER analysis (Figure 1D). For instance, the

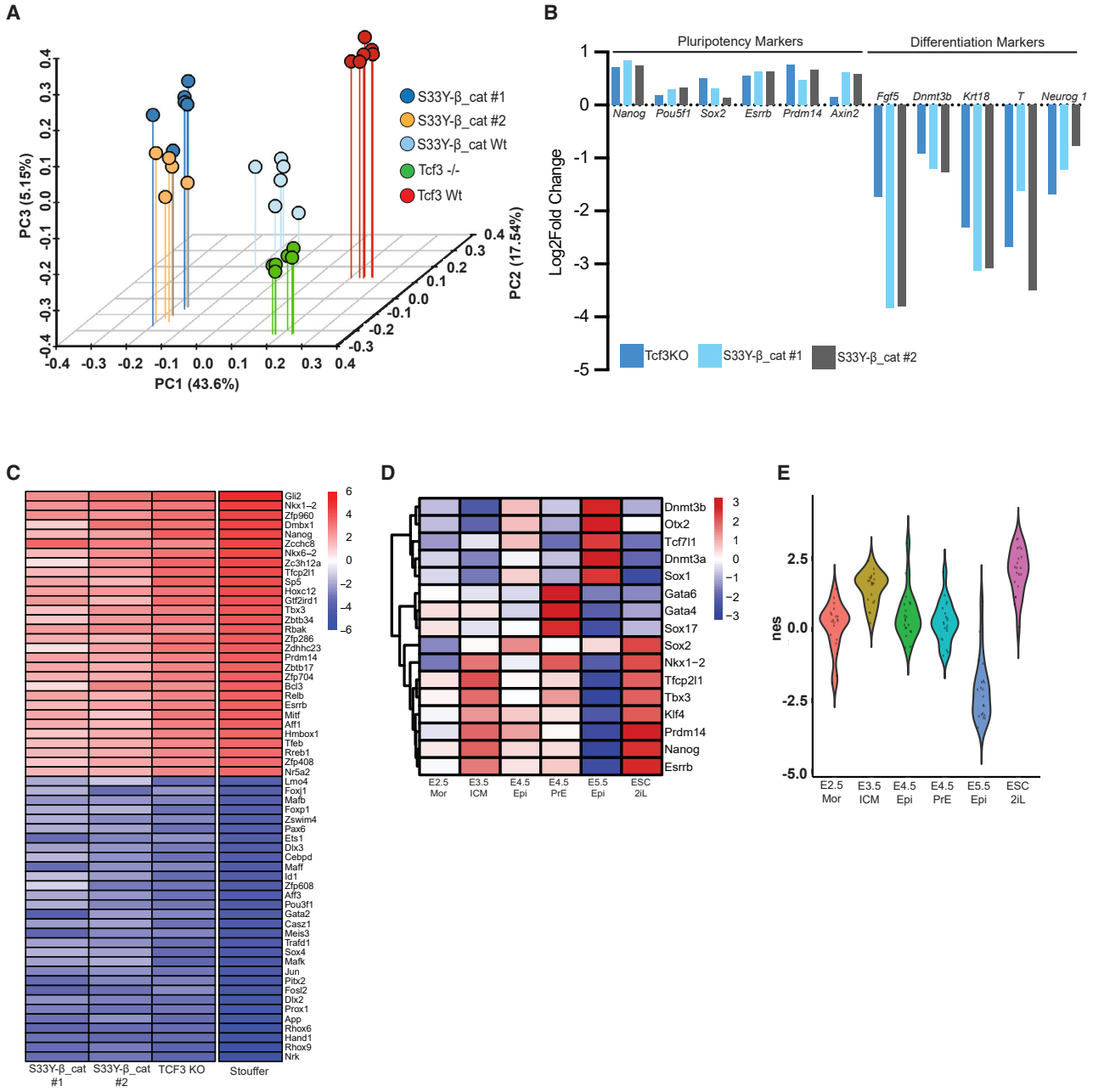

Figure 1. Differential gene expression analysis of β-catenin clones and Tcf3 −/− ESCs and MR analysis

(A) PCA analysis of S33Y-β-catenin #1 (dark blue dots), S33Y-β-catenin #2 (yellow dots), S33Y-β-catenin isogenic E14 WT line (light blue dots), Tcf3 −/− KO (green dots), and Tcf3 isogenic E14tg2a WT line (red dots). *n* = 6 independent experiments per condition.

(B) Differential mRNA expression levels of pluripotency and differentiation genes normalized to the WT. False discovery rate (FDR) < 0.05.

(C) Top active (red) or inactive (blue) MRs in the S33Y-β-catenin #1 or #2 mESC lines or the Tcf3 KO mESC line, ranked according to the cumulative Stouffer score. *n* = 6 independent experiments per condition.

(D) Heatmap showing MR activity across the different early mouse developmental stages (active, red; inactive, blue).

(E) Violin plot showing the activity of the top 18 MRs from Figure 1C (FDR <0.005).

analysis identified *i*) significantly increased activity of established pluripotency factors (e.g., TCFP2L1, TBX3, KLF4, PRDM14, NANOG, and ESRRB) in the E3.5 and E4.5 ICM or in mESCs cultured in 2iLif medium (hereafter, 2iL-mESCs), which maintain a naive ground pluripotency state (Ying et al., 2008); *ii*) significantly increased activity

of the differentiation markers DMT3B, OTX2, DNMT3A, and SOX1 in post-implantation epiblasts, and decreased activity in the preimplantation embryos or in 2iL-mESCs; *iii*) significantly increased activity of TCF7L1 (a transcriptional repressor and Wnt pathway inhibitor) in post-implantation epiblasts, and decreased activity in preimplantation embryo stages and in 2iL-mESCs; and *iv*) significantly increased activity of the PrE markers GATA6, GATA4, and SOX17 in the PrE, as compared to reduced activity in the morula, the ICM, the early Epi, the post-implantation late Epi, or 2iL-mESCs (Figure 1D). Moreover, the top 18 TFs predicted by VIPER were highly active in the ICM of the preimplantation embryos, and 2iLif-mESCs, compared to a significantly reduced activity in the post-implantation Epi (Figure 1E).

Taken together, these data show that VIPER-based MR analysis accurately recapitulates the differential activity of well-established pluripotency and lineage differentiation markers, based on their targets' expression rather than their own expression.

Nkx1-2 regulates mouse embryo development

MR analysis identified the homeobox protein family member NKX1-2 (Rovescalli et al., 2000) as a highly differentially activated MR in the mESC clones #1 and #2, in *Tcf3* KO mESCs, as compared to WT mESCs (Figure 1C), and in the top 8 most-activated factors in the ICM of the mouse preimplantation embryos (Figures 1D and 1E). Given that several homeobox proteins play crucial roles in the zygotic genome activation (ZGA) and preimplantation development in mouse (Eckersley-Maslin et al., 2018), we selected *Nkx1-2* for further experimental validation. Notably, in 2iL-mESCs, in which the Wnt pathway is activated by the GSK3β inhibitor, *Nkx1-2* was upregulated along with the known Wnt target *Axin2*, confirming that NKX1-2 is a Wnt target (Figures S1C and S1D).

To assess whether *Nkx1-2* plays an important physiological role in early embryo development, we analyzed zygotes with an *Nkx1-2* knockdown (KD) mediated by antisense morpholino oligonucleotides (MOs). For this, we microinjected *Nkx1-2*-MOs (or with a randomized sequence as a control; hereafter, CTL-MO) into the cytoplasm of zygotes, which developed *in vitro* until E4.5. In contrast to the normal development of CTL-MO embryos, 70% of the *Nkx1-2* KD embryos (95 of the 136) failed to properly expand the blastocoels and were categorized as "arrested" (Figures 2A and 2B). Of note, most *Nkx1-2* KD embryos that were arrested at the E3.5 stage had formed either no blastocoel (hereafter, a "shrunk" embryo) or only a small blastocoel (hereafter, a "cavity" embryo) (Figure 2A). These MO-mediated KD results were further confirmed using two different small interfering RNA (siRNAs) to mediate the *Nkx1-2* KD: 65.5% (57 of 87) and 95.2% (80 of 84) of embryos injected with *Nkx1-2*-siRNA#1 or with *Nkx1-2*-siRNA#2, respectively, arrested at the morula stage, with some of the embryos arrested at the 2-cell stage (Figures 2C and 2D).

To characterize the developmental defects following *Nkx1-2* KD, we performed single-cell (sc) RNA-seq profiling of CTL-MO or *Nkx1-2*-MO-mediated KD embryos at the morula and blastocyst stages. UMAP analysis of morula stage profiles identified three clusters (MC_0–MC_2), whereby MC_0 contained only CTL-MO cells (red circles) and MC_2, only *Nkx1-2* KD cells (blue triangles). In turn, MC_1 contained mostly *Nkx1-2* KD cells (81%; green triangles) but also CTL-MO cells (green circles), consistent with the heterogeneity of the phenotypic assays (Figure 2E).

Gene ontology (GO) analysis (Zhou et al., 2019) of genes differentially expressed in the MC_2 vs. MC_0 clusters showed strong enrichment of the categories "translation factors," "mRNA transport," and "translation" (Figure 2F). One of the most significantly downregulated genes in *Nkx1-2* KD cells was *Hnrnpa2b1* (Figure S1E), which encodes a nuclear ribonucleoprotein that controls pre-mRNA processing, splicing, RNA nuclear export, and mRNA translation at the ribosomes (Kwon et al., 2019; Liu et al., 2017; Vautier et al., 2001), all of which are essential functions for mammalian embryonic development (Kwon et al., 2019). Other downregulated genes included *Acyp1* (Figure S1F) and *Hnrnph3* (Figure S1G), which also encode proteins involved in controlling RNA splicing and RNA processing. Finally, *Zfas1*, which encodes a ribosome-associated long non-coding RNA involved in translation and RNA processing, was also downregulated (Figure S1H).

scRNA-seq analysis at the blastocyst stage identified four molecularly distinct clusters, termed BC_0–BC_3 (Figure 2G): BC_0 contained only *Nkx1-2* KD cells; BC_2, only CTL-MO cells; and BC_1 and BC_3, a mixture of both cell types. Comparing the GO analysis of BC_0 against all other clusters showed enrichment of genes belonging to the "translation factors" category (Figure 2F). GO analysis of *Nkx1-2* KD cells (BC_0) vs. CTL-MO cells (BC_2) showed strong enrichment for genes related to "formation of a pool of free 40S subunits" (Figure S2A). Overall, at both the morula and blastocyst stages, *Nkx1-2* KD cells showed downregulation of genes and pathways that control ribosome biogenesis, anaphase progression, translation, RNA transport, and focal adhesion (Figures 2H and S2B).

Nkx1-2 is expressed in the nucleoli of preimplantation embryos and controls RNA Pol I nucleolar localization and nucleologenesis

To analyze NKX1-2 expression in the preimplantation embryo stages, we first generated a polyclonal anti-NKX1-2 antibody using a mixture of three peptides (peptides A–C; Figure S3A). A peptide competition assay suggested that

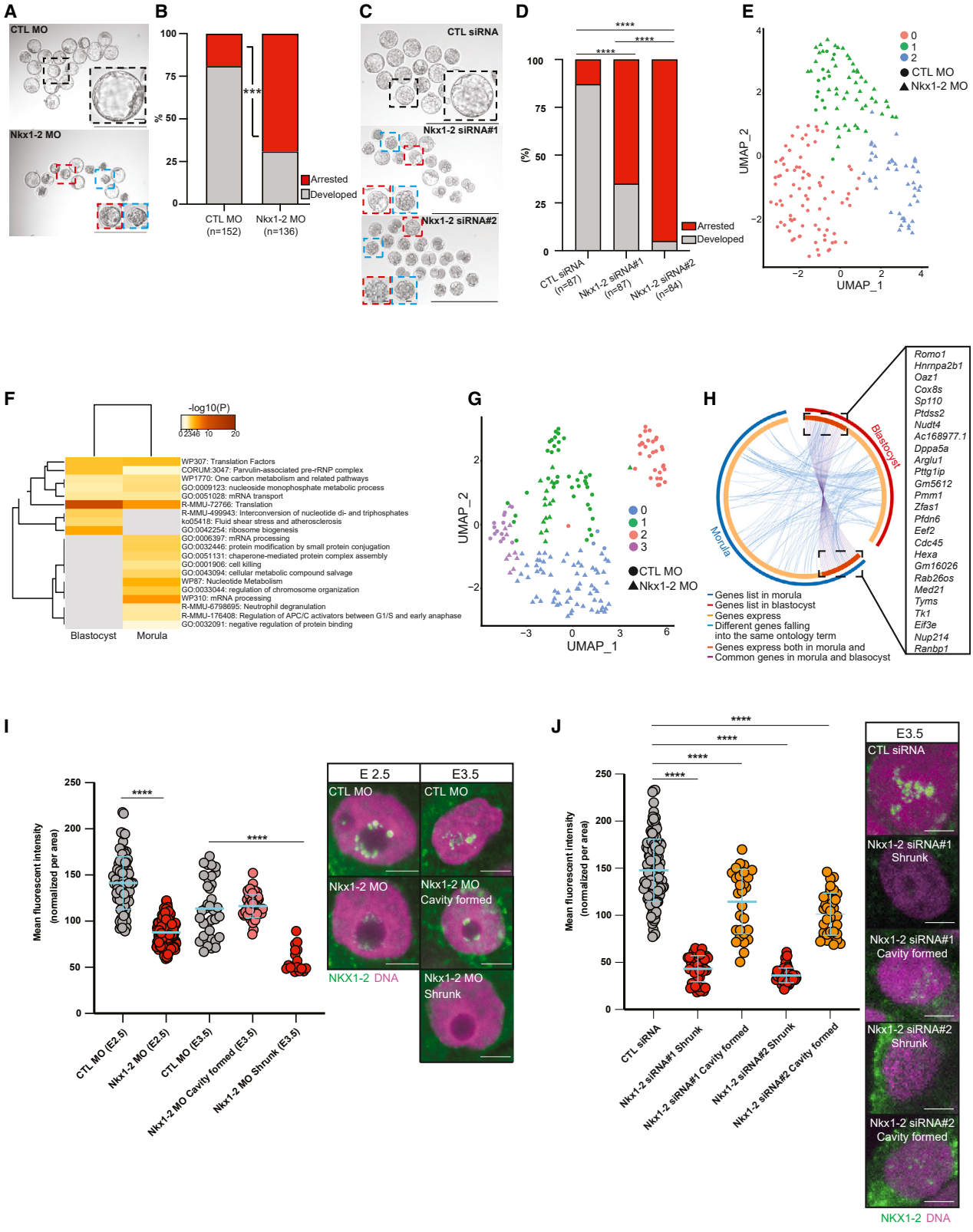

(legend on next page)

the antibody specifically targets the NKX1-2 protein region corresponding to peptide A (Figure S3B). Analyzing germinal vesicle (GV) oocytes and preimplantation embryos (from E0.5 to E3.5) by immunofluorescence staining, we detected NKX1-2 exclusively within foci inside and at the edge of the nucleolus (Figure S3C). Notably, fluorescence was significantly decreased in *Nkx1-2* KD shrunk embryos at E2.5 and E3.5, following either MO-mediated (Figure 2I) or siRNA-mediated KD (Figure 2J), confirming the specificity for NKX1-2.

Growing mouse oocytes from the secondary or preantral follicle display high ribosomal RNA transcription activity, while fully grown oocytes do not show active transcription (Borsos and Torres-Padilla, 2016; Inoue et al., 2008). To determine whether the NKX1-2 localization pattern changed following the initiation of transcriptional activity in the nucleolus, we analyzed NKX1-2 and UBTF (pstream Binding Transcription Factor) (an rRNA TF) by immunofluorescence. In growing oocytes, NKX1-2 and UBTF were expressed across the nucleolus with a high level of co-localization; in contrast, in fully grown oocytes, they were concentrated in foci in the nucleolus, with poor co-localization (Figure 3A). In the preimplantation embryos, as expected, UBTF was expressed after the 2-cell stage, when ZGA takes place (Figure 3B). Of note, while UBTF was not expressed in the zygote at E0.5, NKX1-2 was found only in the maternal pronucleus, suggesting NKX1-2 was maternally inherited. Interestingly, NKX1-2 and UBTF colocalized at all stages of embryo development once UBTF expression was triggered (Figure 3B). These results strongly suggested that NKX1-2 specifically localizes to the nucleoli of mouse oocytes and preimplantation embryos and might thus regulate rRNA biogenesis.

To further investigate a possible role of *Nkx1-2* in rRNA biogenesis, we analyzed nascent RNA synthesis by 5-ethynyl-uridine (EU) incorporation (Wang et al., 2014). The nuclear EU signal was strong in CTL-MO embryos but was significantly reduced in *Nkx1-2* KD embryos (Figures 3C and S3D), suggesting rRNA transcription impairment. Further, using quantitative reverse-transcription PCR (RT-qPCR) to analyze individual embryos, we found that *Nkx1-2* KD embryos had a significantly reduced expression of the pre-ribosomal RNA gene *45S* and showed a trend for reduced expression of the *18S* and *28S* rRNAs

Figure 2. *Nkx1-2* is essential for preimplantation development and regulates translation and ribosome biogenesis

(A) Representative images of embryos injected with CTL-MO (top) or *Nkx1-2*-MO (for KD; bottom). Zoomed images of E3.5 CTL-MO embryos (black line) or of *Nkx1-2* KD embryos with a cavity (red line) or shrunk (blue line) formation. Scale bars, 400 μm (non-zoomed) and 50 μm (zoomed).

(B) Preimplantation development of CTL-MO (n = 152 embryos) or *Nkx1-2* MO-mediated KD embryos (n = 136 embryos), injected at E0.5 zygotes; preimplantation development was evaluated at E4.5. n = 10 independent experiments. ***$p < 0.01$.

(C) Representative images of embryos injected with CTL-siRNA (top), *Nkx1-2* siRNA#1 (middle), or *Nkx1-2* siRNA#2 (bottom). Scale bars, 400 μm.

(D) Preimplantation development of embryos injected with CTL-siRNA (n = 87 embryos), *Nkx1-2* siRNA#1 (n = 87 embryos), or *Nkx1-2* siRNA#2 (n = 84 embryos) at the E0.5 stage and evaluated at E4.5. n = 5 independent experiments. ****$p < 0.0001$.

(E) Single-cell clustering through UMAP (Uniform Manifold Approximation and Projection) dimensionality reduction of morula embryos injected with CTL-MO (n = 96 blastomeres; circles) or *Nkx1-2*-MO (n = 95 blastomeres; triangles). Of the three separate clusters of single cells identified, cluster 0 only contained CTL embryos, and cluster 2, only *Nkx1-2* KD embryos.

(F) GO enrichment analysis by Metascape (https://metascape.org/gp/index.html#/citations/) of significantly (adj. $p < 0.01$) downregulated genes in the *Nkx1-2* KD cluster 2 versus the CTL cluster 0 in the morula stage, or versus all other clusters in blastocyst embryos ($p < 0.05$).

(G) Single-cell clustering through UMAP dimensionality reduction of CTL (n = 86 blastomeres) and *Nkx1-2* MO (n = 91 blastomeres) injected blastocyst embryos. CTL-MO injected cells, circles; *Nkx1-2* KD cells, triangles. Four separate clusters of single cells were identified.

(H) Circos plot showing downregulated genes and overlapped genes between morula and blastocyst embryos after *Nkx1-2*-MO injection. Downregulated genes in *Nkx1-2* KD embryos were identified by comparing the marker genes of MC_0 vs. MC_2 (for morula) and BC_0 vs. BC_1, $_{-2}$, and $_{-3}$ (for blastocyst). Each arc in the plot represents a gene list, whereby each gene has a spot on the arc. Dark orange represents genes expressed in both morula and blastocyst; light orange, genes expressed uniquely in one. Purple lines link the same genes that are expressed in both morula and blastocyst, and blue lines link different genes falling into the same ontology term.

(I and J) Mean fluorescent intensity (normalized by area) of NKX1-2 in CTL-MO or *Nkx1-2* KD (MO-mediated) embryos (I), or in CTL-siRNA or *Nkx1-2* KD (siRNA-mediated) embryos (J). For (I), the following blastomeres were analyzed: CTL-MO E2.5 (gray dots, n = 85 blastomeres), *Nkx1-2* KD E2.5 (red dots, n = 178 blastomeres), CTL-MO E3.5 (gray dots, n = 36 blastomeres), *Nkx1-2* KD cavity E3.5 (pink dots, n = 48 blastomeres), and *Nkx1-2* KD shrunk E3.5 (red dots, n = 17 blastomeres). n = 3 independent experiments. Representative images of NKX1-2 immunostaining are shown for E2.5 and E3.5 CTL-MO embryos and *Nkx1-2* KD embryos (right). For (J), the following blastomeres were analyzed in E3.5 embryos: CTL-siRNA (gray dots, n = 152 blastomeres), *Nkx1-2* siRNA#1 KD shrunk (red dots, n = 43 blastomeres), *Nkx1-2* siRNA#1 KD cavity (orange dots, n = 29 blastomeres), *Nkx1-2* siRNA#2 KD shrunk (red dots, n = 64 blastomeres), and *Nkx1-2* siRNA#2 KD cavity (orange dots, n = 35 blastomeres). n = 3 independent experiments. Representative images of NKX1-2 immunostaining are shown for E3.5 CTL-siRNA or *Nkx1-2* KD embryos (right). For both (I, J), green, NKX1-2 (anti-NKX1-2); magenta, DNA (DRAQ5). Scale bars, 5 μm.

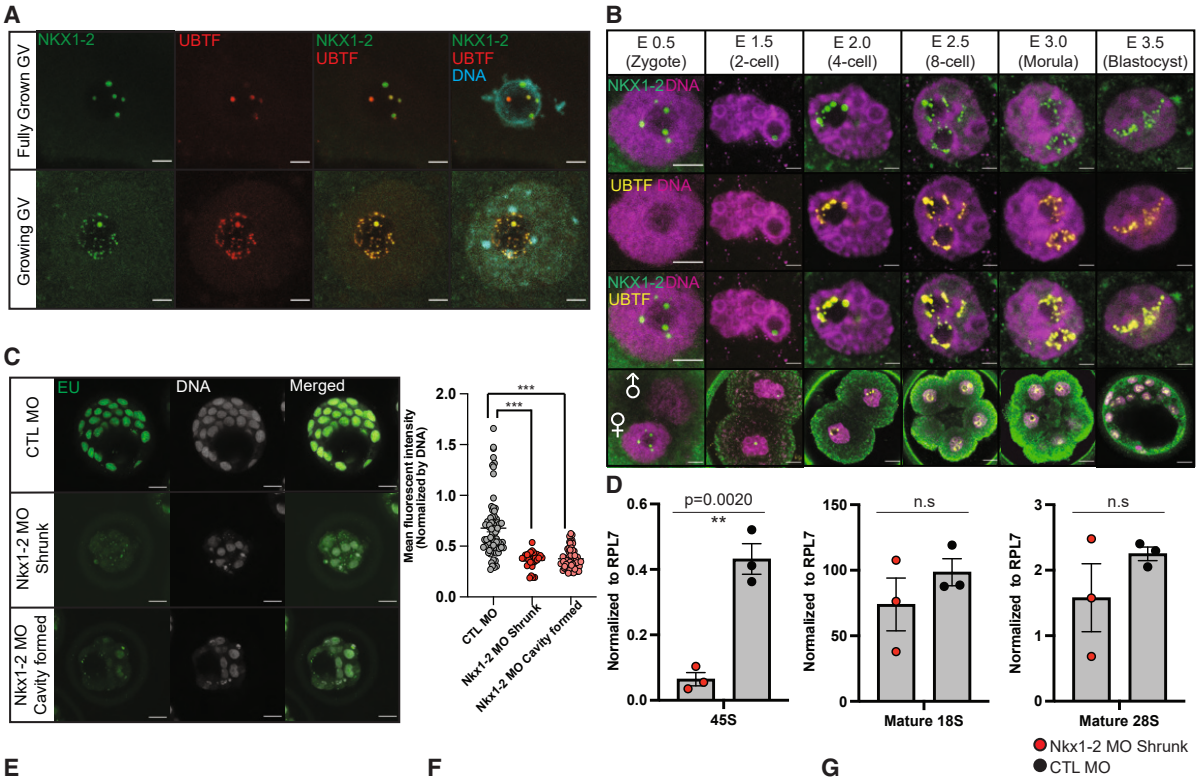

(legend on next page)

(Figure 3D), further suggesting rRNA transcription impairment. Thus, we next investigated RNA POL I localization. We found that NKX1-2 and POL I colocalized in the nucleoli of CTL-MO embryos from the 2-cell until blastocyst stages (Figures 3E–3H). Strikingly, however, the POL I signal was strongly reduced or absent in the nucleoli of *Nkx1-2* KD embryos (from the 2-cell to blastocyst stage) (Figures 3E–3H for the MO-mediated KD, and Figure S3E for the siRNA#1- or siRNA#2-mediated KD), indicating that POL I was either not imported into nucleoli or not correctly assembled, and thus not retained in the nucleolus, in *Nkx1-2* KD embryos.

Nucleologenesis takes place progressively during mouse preimplantation development (Fulka and Aoki, 2016; Kone et al., 2016), and the formation of mature nucleoli is essential for rRNA biogenesis (Boisvert et al., 2007). To determine whether nucleologenesis was impaired by *Nkx1-2* KD, we next analyzed the nucleoli of *Nkx1-2* KD or CTL-MO embryos at the morula (E2.5) and blastocyst (E3.5) stages, using transmission electron microscopy (TEM). In *Nkx1-2* KD blastocyst embryos, we observed condensed nucleoli (Figure 3I, yellow asterisk) and disrupted nucleoli (Figure 3I, black arrow) in some blastomeres. These results strongly suggest that NKX1-2 is essential for proper nucleologenesis in preimplantation embryos.

Nkx1-2 KD triggers severe chromosome missegregation and mitotic division errors during preimplantation development

Protein-protein interaction analysis of the MO-mediated *Nkx1-2* KD embryos revealed that the anaphase progression complex was deregulated (Figures 2F and S2B; MCODE_2). Based on this and the observation that NKX1-2 appeared to play a major role in ribosomal RNA synthesis and translation, we studied for possible defects in mitotic division by comparing live-cell imaging of *Nkx1-2* KD vs. CTL-MO embryos. We observed binucleation and severe lagging chromosomes in *Nkx1-2* KD embryos (Figure 4A and Videos S1, S2, and S3), starting in the 2- to 4-cell transition (Figure 4A, *Nkx1-2* KD binucleation and lagging).

Robust bipolar spindle formation and precise attachment of kinetochore-microtubules (K-MTs) are essential for accurate cell division and correct chromosome segregation (Hassold and Hunt, 2001; Nakagawa and FitzHarris, 2017). Interestingly, NKX1-2 also colocalized with UBTF on mitotic chromosomes (Figure S3F). To assess whether binucleation and chromosome segregation errors were induced due to incorrect spindle formation and/or K-MT attachment in *Nkx1-2* KD embryos, we performed a K-MT attachment assay in embryos synchronized in mitosis (Watanabe et al., 2016). Embryos were synchronized at the E1.0 (1- to 2-cell transition) and E2.0 stages (4- to 8-cell transition). After a cold shock treatment, we found that several *Nkx1-2* KD embryos had multipolar spindles (55.6%, 10 out of 18) and disorganized microtubules (MTs) (27.8%, 5 out of 18) (Figures 4B and 4C) and an increased number of chromosomes with merotelic attachment (28.7% vs. 66.3%, Figures 4D–4F).

The *Nkx1-2* KD embryos contained many micronuclei (asterisk in Figure 4A, and yellow arrows in Figure 4G), a hallmark of segregation errors and chromosome instability (Fenech et al., 2011), further suggesting chromosome missegregation. All *Nkx1-2* KD embryos showed a significantly reduced number of blastomeres as compared to CTL-MO embryos (Figure 4H); specifically, the average blastomere number at E3.5 for CTL-MO embryos was 57.7 ± 4.7, for *Nkx1-2* KD shrunk embryos, 17.3 ± 3.9 ($p < 0.0001$), and for *Nkx1-2* KD cavity embryos, 21.6 ± 2.5 ($p < 0.0001$). Moreover, blastomeres in *Nkx1-2* KD embryos

Figure 3. NKX1-2 colocalizes with UBTF and regulates rRNA expression in mouse oocytes and preimplantation embryos

(A) Representative images of NKX1-2 and UBTF showing co-localization in growing mouse germinal vesicle (GV) oocytes but not in fully developed oocytes. Green, NKX1-2 (anti-NKX1-2); red, UBTF (anti-UBTF); cyan, DNA (DRAQ5). Scale bars, 5 μm.

(B) Representative images of NKX1-2 and UBTF in preimplantation embryos. UBTF is expressed starting from the 4-cell stage and then always colocalizes with NKX1-2. Green, NKX1-2 (anti-NKX1-2); yellow, UBTF (anti-UBTF); magenta, DNA (DRAQ5). Scale bars, 5 μm (zygotes), 2 μm (zoomed), or 10 μm (low magnification).

(C) Representative images of EU incorporation and mean fluorescent intensity in *Nkx1-2* KD or CTL-MO embryos. Green, EU; gray, DNA (DRAQ5). The EU signal was significantly reduced in *Nkx1-2* KD embryos, both with shrunk (red dots, $n = 29$ blastomeres) or cavity (pink dots, $n = 58$ blastomeres) formation, as compared to CTL-MO embryos (gray dots, $n = 70$ blastomeres). $n = 3$ independent experiments. ***$p < 0.01$. Scale bars, 20 μm.

(D) RT-qPCR of *45S*, mature *18S*, and mature *28S* in *Nkx1-2* KD and CTL-MO embryos. Data are presented as mean ± SEM. $n = 3$ independent experiments. p values, t test.

(E–H) Representative images of NKX1-2 and RNA POL I immunostaining of CTL-MO or *Nkx1-2* KD (MO-mediated) embryos, at E1.5 (2-cell) (E), E2.0 (4-cell) (F), E2.5 (morula) (G), or E3.5 (blastocyst) (H). Green, NKX1-2 (anti-NKX1-2); red, RNA POL I (anti-RPA194); gray, DNA (DRAQ5). Scale bars, 3 μm.

(I) Representative images of transmission electron microscopy images of *Nkx1-2* KD or CTL-MO embryos at E2.5 (morula) or E3.5 (blastocyst). In the low-magnification images, red asterisks, hollows; yellow asterisks, condensed nucleoli; black arrows, disrupted nucleoli; and yellow arrows, tight junctions. Scale bars, 5 μm.

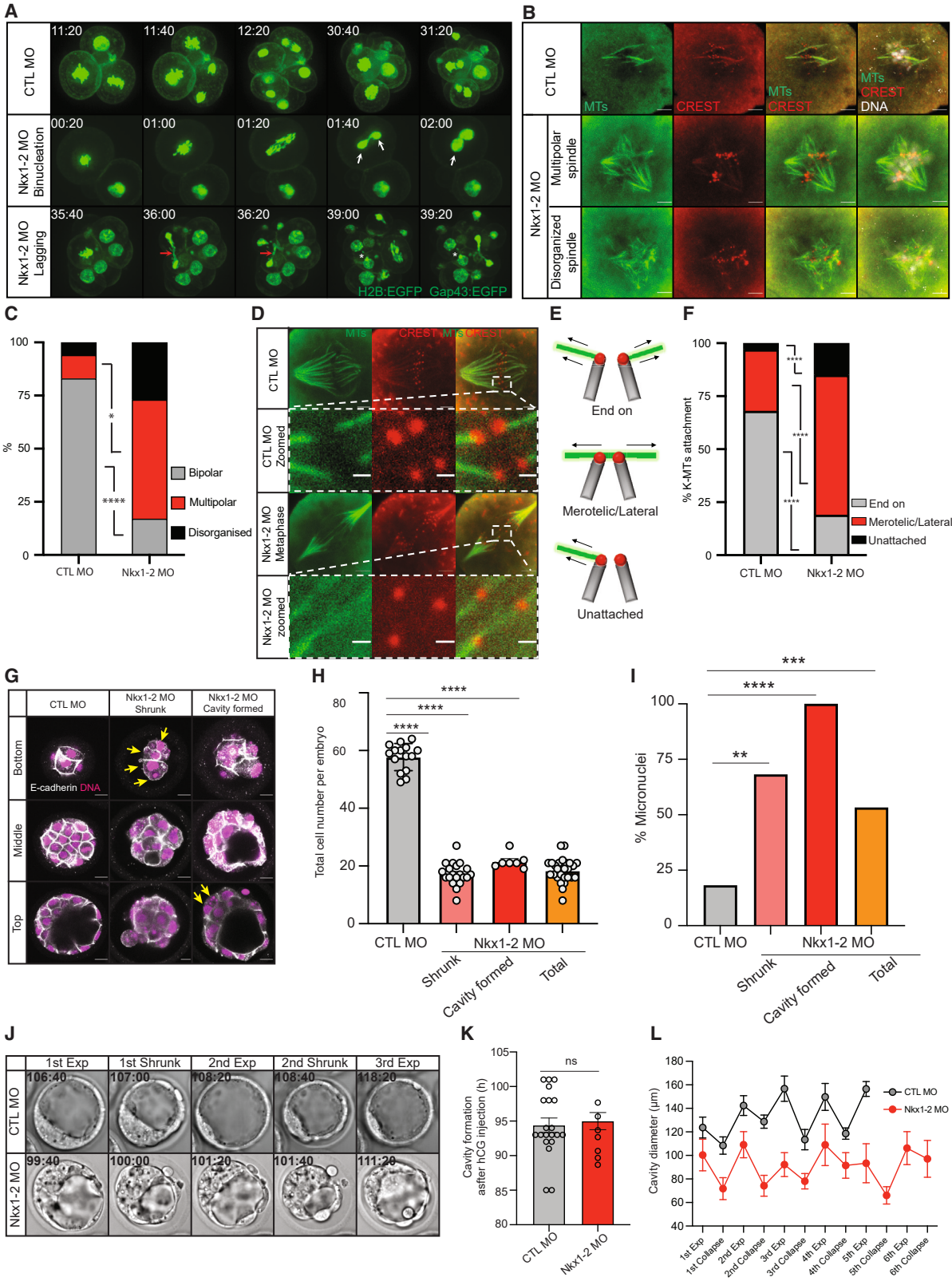

(legend on next page)

were multi-nucleated (Figures 4G and 4I), further suggesting a defect during cell division. Taken together, these data show that NKX1-2 transcriptional activity is essential for accurate chromosome segregation and proper mitotic division during preimplantation development.

The blastocoel formation cycle is impaired in *Nkx1-2* KD embryos

As shown earlier, *Nkx1-2* KD induced incomplete blastocoel formation in a large majority of the embryos, as well as arrest during preimplantation development (Figures 2A–2D). Moreover, we observed that *Nkx1-2* KD embryos showed highly significant blastomere number reduction and chromosome segregation defects (Figures 4A–4I), both of which impair embryo size and development. Consistent with previous reports (Chan et al., 2019), CTL-MO embryos increased their size by repeating the blastocoel expansion-collapse cycle and finally hatched after several cycles (Figures 2A, 2C, and 4J, and Video S4). The timing of the first blastocoel formation was comparable in CTL-MO and *Nkx1-2* KD embryos (mean ± SD for CTL-MO embryos, 94:43 ± 4:40 h; *Nkx1-2* KD embryos, 95:20 ± 3:10 h; Figure 4K). However, although blastocoel expansion-collapse cycles were observed in some of the *Nkx1-2* KD embryos, the cycle was not associated with an increase in embryo size (Figure 4L and Video S5), as assessed by measuring the cavity's diameter (Figure 4L; CTL-MO embryos: 1st expansion, 123.76 ± 40.12 μm, last expansion 156.76 ± 33.99 μm; *Nkx1-2* KD embryos: 1st expansion, 100.41 ± 35.72 μm, last expansion 106.20 ± 34.36 μm, mean ± SD). Some embryos showed no or only minimal re-expansion of the blastocoel for several hours, finally terminating with blastocoel collapse (Figure S3G and Video S6). These results indicated that the blastocoel expansion-collapse process severely failed in *Nkx1-2* KD mouse embryos.

TJs are not sealed in *Nkx1-2* KD embryos

The proper formation and sealing of TJs, which regulate the diffusion of solutes and ions between the apical and basolateral plasma membranes (Tsukita et al., 2001), are essential for blastocoel formation during preimplantation development (Eckert and Fleming, 2008). To test whether impaired blastocoel formation in *Nkx1-2* KD embryos was due to improper TJ sealing, we first immunostained the TJ proteins ZO-1 and VINCULIN in CTL-MO and *Nkx1-2* KD embryos. While both ZO-1 and VINCULIN were homogenously expressed in CTL-MO embryos, neither protein was expressed in *Nkx1-2* KD embryos (Figures 5A and 5B).

To directly assess whether TJs were properly sealed, we performed a TJ permeability assay by incubating CTL-MO and *Nkx1-2* KD embryos in a rhodamine-dextran medium for 10 min and then checking for rhodamine-dextran influx into the blastocoels. Indeed, we observed that

Figure 4. *Nkx1-2* KD leads to severe chromosome missegregation and mitotic division errors

(A) Time-lapse images of *Nkx1*-2 KD and CTL-MO embryos. Binucleation, white arrow; lagging chromosomes, red arrow; micronucleoli, white asterisk. Chromosomes and plasma membrane were visualized by H2B:EGFP and Gap43:EGFP, respectively.

(B–D) Analyses of CTL-MO or *Nkx1-2* KD embryos after nocodazole synchronization, cold shock, and heating (at E2.0) for 15 min (B, C) or 20 min (D). In (B), representative images show that CTL-MO embryos (top) had normal microtubules (MTs), while *Nkx1-2* KD embryos frequently had multipolar spindles (middle) or disorganized spindle formation (bottom). In (C), spindle formation was categorized as bipolar (gray), multipolar (red), or disorganized (black). *Nkx1-2* KD; n = 18 spindles, CTL-MO; n = 18 spindles, n = 3 independent experiments. *p = 0.0116, ****p = 0.0002. In (D), representative images show that bipolar spindles had end-on kinetochore-MT (K-MT) attachment in CTL-MO embryos (zoomed) but frequently showed merotelic/lateral K-MT attachment in *Nkx1-2* KD embryos (*Nkx1-2* MO, zoomed). For (B) and (D): green, microtubules (anti-β-TUBULIN); red, kinetochores (anti-CREST); gray, DNA (DRAQ5). Scale bars, 5 μm (for non-zoomed) or 1 μm (for zoomed images).

(E) K-MT attachment was classified into three categories: end-on, merotelic/lateral, or unattached. Green, MTs; red, kinetochore; gray, chromatid.

(F) Quantification of K-MT attachment in CTL-MO or *Nkx1-2* KD embryos. Gray, end-on; red, merotelic/lateral; black, unattached. *Nkx1-2* KD; n = 36 embryos, CTL-MO; n = 18 embryos, n = 3 independent experiments. ****p = 0.0002.

(G) Representative images (at E3.5) of mitotic division in CTL-MO embryos (left) or *Nkx1-2* KD embryos (middle and right). Images show different z stacks of a single embryo. Micronuclei were present in the *Nkx1-2* KD shrunk (middle, yellow arrows) and cavity (right, yellow arrows) embryos. Gray, E-cadherin; magenta, DNA (DRAQ5). Scale bars, 10 μm.

(H and I) Quantification of the total number of blastomeres (H) or micronuclei (I) in CTL-MO (n = 15 embryos) or *Nkx1-2* KD (shrunk, n = 20 embryos; cavity, n = 7 embryos; total, n = 27 embryos) E3.5 embryos. n = 3 independent experiments.

(J) Time-lapse images of blastocoel formation in CTL-MO or *Nkx1-2* KD embryos. Cavity expansion was observed after each expansion/collapse cycle in CTL-MO embryos but not in *Nkx1-2* KD embryos.

(K) Timings of the first blastocoel formation in CTL-MO (n = 20 embryos) or *Nkx1-2* KD (n = 7 embryos) embryos. Only embryos showing more than five expansion/collapse cycles were analyzed. n = 3 independent experiments.

(L) Quantification of cavity diameter in CTL-MO (n = 20 embryos) or *Nkx1-2* KD (n = 7 embryos) embryos. Cavity diameter was measured at each cycle of expansion (mean ± SEM). n = 3 independent experiments.

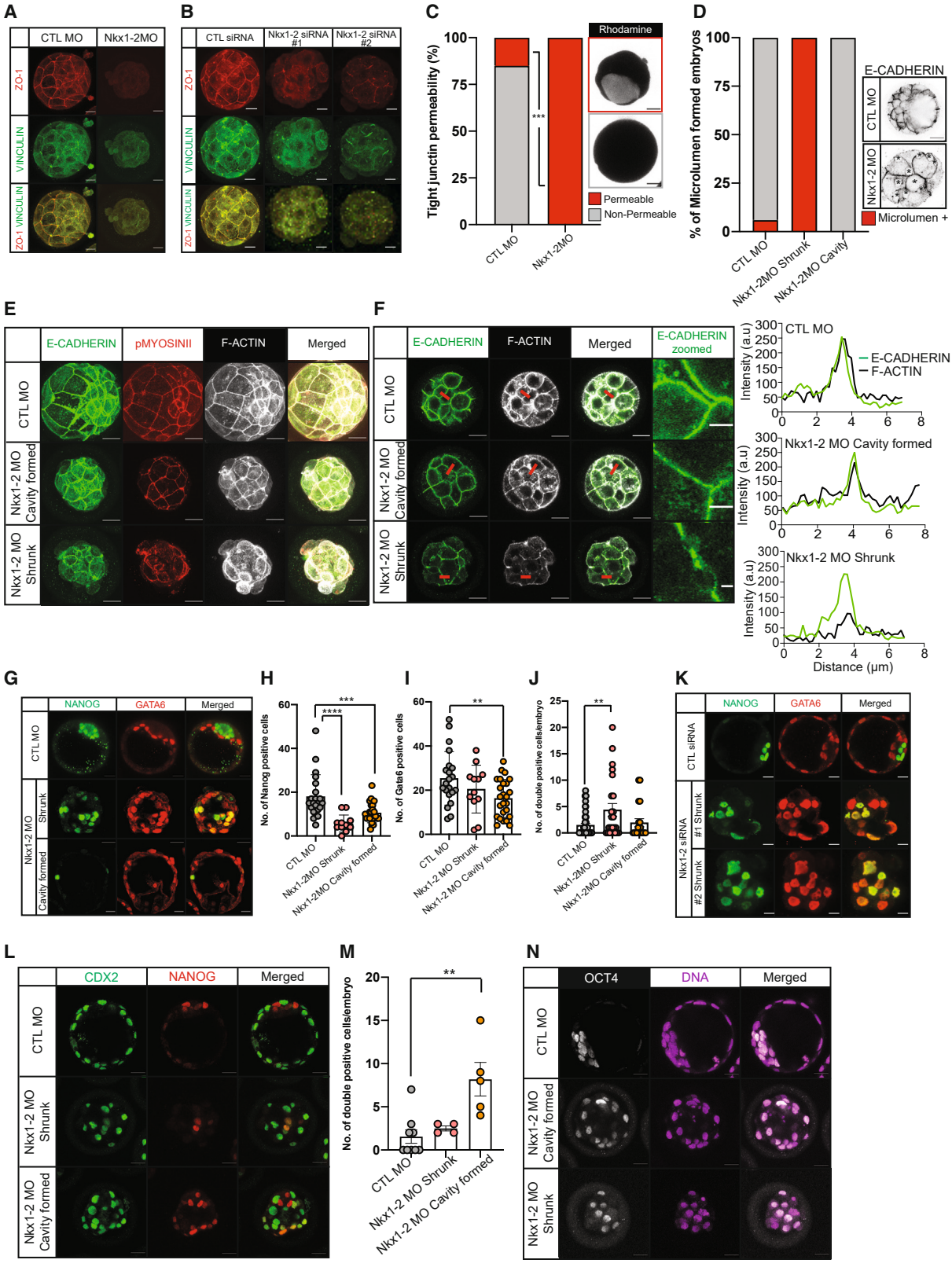

(legend on next page)

rhodamine-dextran infiltrated into the blastocoel in all 12 *Nkx1-2* KD embryos (100%) (Figure 5C) but only in 4 of 26 CTL-MO embryos (15%) (Figure 5C). TEM analyses also confirmed that TJs were not sealed in *Nkx1-2* KD embryos (Figure 3I; TJs, yellow arrow). We concluded that TJ sealing was dysregulated in *Nkx1-2* KD embryos, resulting in increased embryo permeability that affected blastocoel formation and thus preimplantation development.

Microlumen coarsening is impaired, and actomyosin is chaotically expressed, in *Nkx1-2* KD embryos

Formation of the blastocoel, which is a fluid-filled lumen, requires the generation of hundreds of microlumens at the external membranes of neighboring blastomeres as well as microlumen coarsening (Arroyo and Trepat, 2019; Dumortier et al., 2019). As *Nkx1-2* KD embryos showed severe defects in blastocoel formation and TJ permeability, we asked whether they also had impaired microlumen coarsening. Notably, all of the E3.5 *Nkx1-2* KD embryos with a shrunk formation (20 of 20) showed the presence of microlumens at the cell-to-cell blastomere adhesion sites, while only 1 of 16 E3.5 CTL-MO embryos (6.3%) showed visible microlumens (Figure 5D, asterisk). In sharp contrast, none of the *Nkx1-2* KD cavity embryos showed microlumens (0 of 10; Figure 5D).

Microlumen coarsening is controlled by cell adhesion and cell contractility programs (Arroyo and Trepat, 2019; Dumortier et al., 2019). Of note, our scRNA-seq analysis showed that the gene encoding the myosin-binding subunit of myosin phosphatases (*Ppp1r12a*) was specifically downregulated in the *Nkx1-2* KD cell cluster (Figure S3H). Consistently, network-based gene set enrichment analysis using protein-protein interactions (Bader and Hogue, 2003) revealed that "focal adhesion" and "regulation of actin cytoskeleton" genes were downregulated in the *Nkx1-2* KD cell clusters (Figure S2B, MCODE_8). We next investigated whether cell adhesion and/or cell contractility programs were dysregulated in *Nkx1-2* KD embryos by analyzing the immunostaining of E-CADHERIN, which regulates cell adhesion, and of PHOSPHORYLATED MYOSIN LIGHT CHAIN II (p-MYOSIN II) and F-ACTIN, which control cell contractility (Maitre et al., 2015; Samarage et al., 2015). While *Nkx1-2* KD cavity embryos and CTL-MO embryos showed co-localization of all three proteins,

Figure 5. Severe impairment of TJ sealing, actin/myosin expression, and cell fate specification in *Nkx1-2* KD embryos

(A and B) Representative images of the TJ proteins ZO-1 and vinculin in (A) CTL-MO and *Nkx1-2* KD (MO-mediated) embryos; and (B) CTL-siRNA or *Nkx1-2* KD (siRNA-mediated) embryos. ZO-1 and vinculin were not detected in *Nkx1-2* KD embryos in either KD condition. Red, ZO-1; green, vinculin. Scale bars, 15 μm.

(C) Representative images of E3.5 embryos with *Nkx1-2* KD (MO-mediated) (top) or CTL-MO (bottom), and incubated in medium supplemented with rhodamine-dextran (3,000 MW). Only cavity embryos were analyzed (CTL-MO, $n = 26$ embryos; *Nkx1-2* KD, $n = 12$ embryos). $n = 2$ independent experiments. Scale bars, 20 μm.

(D) Representative images and quantification of microlumen coarsening in CTL-MO ($n = 16$ embryos) or *Nkx1-2* KD (shrunk, $n = 20$ embryos; cavity, $n = 10$ embryos) embryos at E3.5. Microlumens are indicated with black asterisks. Gray, E-CADHERIN. Scale bar, 20 μm. Red indicates embryos with numerous microlumens. $n = 3$ independent experiments.

(E) Representative immunofluorescence images of E-CADHERIN, F-ACTIN, and MYOSIN in CTL-MO or *Nkx1-2* KD embryos (at E3.5). Green, E-CADHERIN; red, MYOSIN (using anti-PHOSPHO-MYOSIN LIGHT CHAIN 2 [Thr18/Ser19]); gray, F-ACTIN (using anti-PHALLOIDIN). Scale bars, 20 μm.

(F) Representative immunofluorescence images of E-CADHERIN and ACTIN in CTL-MO or *Nkx1-2* KD embryos (at E3.5). Green, E-CADHERIN; gray, F-ACTIN (anti-PHALLOIDIN). Line scans were quantified in the middle areas of embryos (red line), and results are shown in the plots (CTL-MO, 25 embryos; *Nkx1-2* KD shrunk, 16 embryos; *Nkx1-2* KD cavity, 7 embryos). Scale bars, 20 μm; for zoomed images, 5 μm for CTL-MO and *Nkx1-2* KD cavity, and 2 μm for *Nkx1-2* KD shrunk. $n = 3$ independent experiments.

(G) Representative immunofluorescence images of NANOG (epiblast cells) and GATA6 (primitive endoderm cells) in CTL-MO or *Nkx1-2* KD embryos (E4.5). Green, NANOG (anti-NANOG); red, GATA6 (anti-GATA6). Scale bars, 20 μm.

(H and I) Quantification of the number of NANOG-positive cells (H) or GATA6-positive cells (I) in CTL-MO ($n = 21$ embryos) or *Nkx1-2* KD (shrunk, $n = 12$ embryos; cavity, $n = 25$ embryos) embryos (at E4.5). $n = 3$ independent experiments. $^{****}p < 0.0001$, $^{***}p < 0.001$, $^{**}p < 0.01$.

(J) Quantification of the number of NANOG and GATA6 double-positive cells in CTL-MO ($n = 49$ embryos) or *Nkx1-2* KD (shrunk, $n = 24$ embryos; cavity, $n = 20$ embryos) embryos (at E4.5). $n = 3$ independent experiments. $^{**}p < 0.01$.

(K) Representative immunofluorescence images of NANOG (epiblast cells) and GATA6 (primitive endoderm cells) in CTL-siRNA and *Nkx1-2* KD (siRNA-mediated) embryos (E4.5). Green, NANOG (anti-NANOG); red, GATA6 (anti-GATA6). Scale bars, 20 μm.

(L) Representative immunofluorescence images of CDX2 (trophectoderm cells) and NANOG (epiblast cells) in CTL-MO and *Nkx1-2* KD (MO-mediated) embryos (at E3.5). Green, CDX2 (anti-CDX2); red, NANOG (anti-NANOG). Scale bars, 20 μm.

(M) Quantification of the number of CDX2 (trophectoderm cells) and NANOG (epiblast cells) double-positive cells in CTL-MO ($n = 9$ embryos) and *Nkx1-2* KD (shrunk, $n = 4$ embryos; cavity, $n = 5$ embryos) embryos at E3.5. $n = 2$ independent experiments. $^{**}p < 0.01$.

(N) Representative immunofluorescence images of OCT4 (ICM marker) in CTL-MO or *Nkx1-2* KD embryos (at E3.5). Gray, OCT4 (anti-OCT4); magenta, DNA (DRAQ5). Scale bars, 20 μm.

Nkx1-2 KD shrunk embryos showed disorganized expression patterns of p-MYOSIN II and F-ACTIN (and, to a lesser degree, of E-CADHERIN) (Figure 5E). With respect to fluorescence intensity, 23 out of 25 CTL-MO embryos (92.0%) showed comparable E-CADHERIN and F-ACTIN fluorescence intensity peaks (Figure 5F). In contrast, the intensity of F-ACTIN fluorescence peaks was lower in 13 out of 16 (81.2%) of the *Nkx1-2* KD shrunk embryos, but it was partially recovered in 4 out of 7 of the cavity *Nkx1-2* KD embryos (57.1%) (Figure 5F). Further, in *Nkx1-2* KD shrunk embryos, E-CADHERIN had a similar fluorescence intensity as in CTL-MO embryos but did not appear to continuously line the cells' adhesion sites, likely because of the lack of coarsening of the microlumens (Figure 5F, E-CADHERIN zoomed). Moreover, countless hollows were formed in the cytoplasm of the *Nkx1-2* KD morula and blastocyst embryos (Figure 3I, low magnification, red asterisks).

Cell fate specification is impaired in the ICM of *Nkx1-2* KD embryos

Blastocoel expansion is critical for cell fate specification of Epi and PrE cells in the ICM of mouse blastocysts (Chan and Hiiragi, 2020; Ryan et al., 2019). Thus, we asked whether cell fate specification in the ICM was affected in *Nkx1-2* KD embryos by assessing the expression of established lineage markers, including *Nanog* for Epi, and *Gata6* for PrE. In CTL-MO embryos, NANOG-positive cells were localized in the middle of ICM, and GATA6-positive cells were below NANOG-positive ones, as expected (Figure 5G). However, both NANOG- and GATA6-positive cells were randomly localized throughout the entire *Nkx1-2* KD embryos, and many blastomeres co-expressed both genes (Figure 5G). Importantly, both shrunk and cavity embryos showed aberrant cell fate specification. Moreover, the number of blastomeres positive for NANOG (in shrunk or cavity embryos) or for GATA6 (in cavity embryos) was significantly lower in *Nkx1-2* KD embryos than in CTL-MO embryos (Figures 5H and 5I). We also found an increased number of NANOG and GATA6 double-positive blastomeres in *Nkx1-2* KD shrunk embryos (Figure 5J). Confirming the MO-mediated KD results, a comparable or even more severe phenotype of aberrant cell fate specification was observed in siRNA #2-mediated *Nkx1-2* KD shrunk embryos (Figures 5K, S3I, and S3J).

Next, we examined additional pluripotency marker genes in MO-mediated *Nkx1-2* KD embryos, such as *Cdx2* (trophectoderm marker) and *Oct4* (ICM marker). As expected, CDX2-positive cells were exclusively localized in the trophectoderm of the E3.5 CTL-MO embryos (Figure 5L). In sharp contrast, CDX2-positive cells were found across the entirety of the shrunk or cavity *Nkx1-2* KD embryos. Of note, many blastomeres co-expressed both NANOG and CDX2 in the *Nkx1-2* KD embryos (Figures 5L and 5M). The OCT4 expression pattern in *Nkx1-2* KD embryos was also affected. Indeed, OCT4-positive cells were localized only to the ICM in the CTL-MO embryos but were expressed in the large majority of cells in the *Nkx1-2* KD embryos (Figure 5N). Thus, these results showed that defective blastocoel formation upon *Nkx1-2* KD was coupled with aberrant cell fate specification in the blastocyst embryos.

Microinjection of *Nkx1-2* mRNA partially rescues developmental arrest and ribosome biogenesis in *Nkx1-2* KD embryos

Finally, we asked whether developmental arrest of *Nkx1-2* KD embryos could be rescued by ectopic *Nkx1-2* mRNA expression. We thus microinjected MO-insensitive *Nkx1-2* mRNA into (MO-mediated) *Nkx1-2* KD zygotes. While only 19% of embryos hatched after *Nkx1-2* KD, developmental arrest and blastocoel formation were significantly rescued (45% hatching) by mRNA injection (Figure 6A); moreover, NKX1-2 and POL I were expressed in the rescued embryos (Figures 6B–6D). We next assessed whether cell fate specification could be rescued by *Nkx1-2* mRNA overexpression. Both NANOG- and GATA6-positive cells were correctly localized in the rescued embryos (Figure 6E). In addition, NANOG-positive cells and total cell numbers were significantly increased in the rescued embryos (Figures 6E–6G). As we observed rRNA transcription impairment, we wondered whether P53 expression would be triggered, as is seen after ribosomal stress (such as that induced by UV irradiation or transcription inhibition; Lindstrom et al., 2022). P53 was not expressed in CTL-MO or *Nkx1-2* rescued embryos, but it was significantly expressed in *Nkx1-2* KD embryos, suggesting ribosome impairment in these embryos (Figure S3K). We then investigated whether the reduction of rRNA biogenesis gene expression in *Nkx1-2* KD embryos was rescued by *Nkx1-2* mRNA expression. Indeed, RT-qPCR results indicated that expression of the gene encoding the pre-ribosomal RNA *45S* was significantly reduced in *Nkx1-2* KD embryos but was partially recovered in the rescued embryos (Figure 6H). Finally, we transferred CTL-MO, *Nkx1-2* KD, and *Nkx1-2* rescued embryos into foster female mice to assess their full-term development. Healthy pups were born from foster mothers implanted with CTL-MO or rescued embryos but not from those with *Nkx1-2* KD embryos, suggesting that the *Nkx1-2* mRNA rescue likewise overcame the *Nkx1-2* KD developmental defects (Figure 6I).

DISCUSSION

VIPER-based MR analysis provides a valuable and extensively validated approach to identify direct, mechanistic regulators of biological functions (Alvarez et al., 2016).

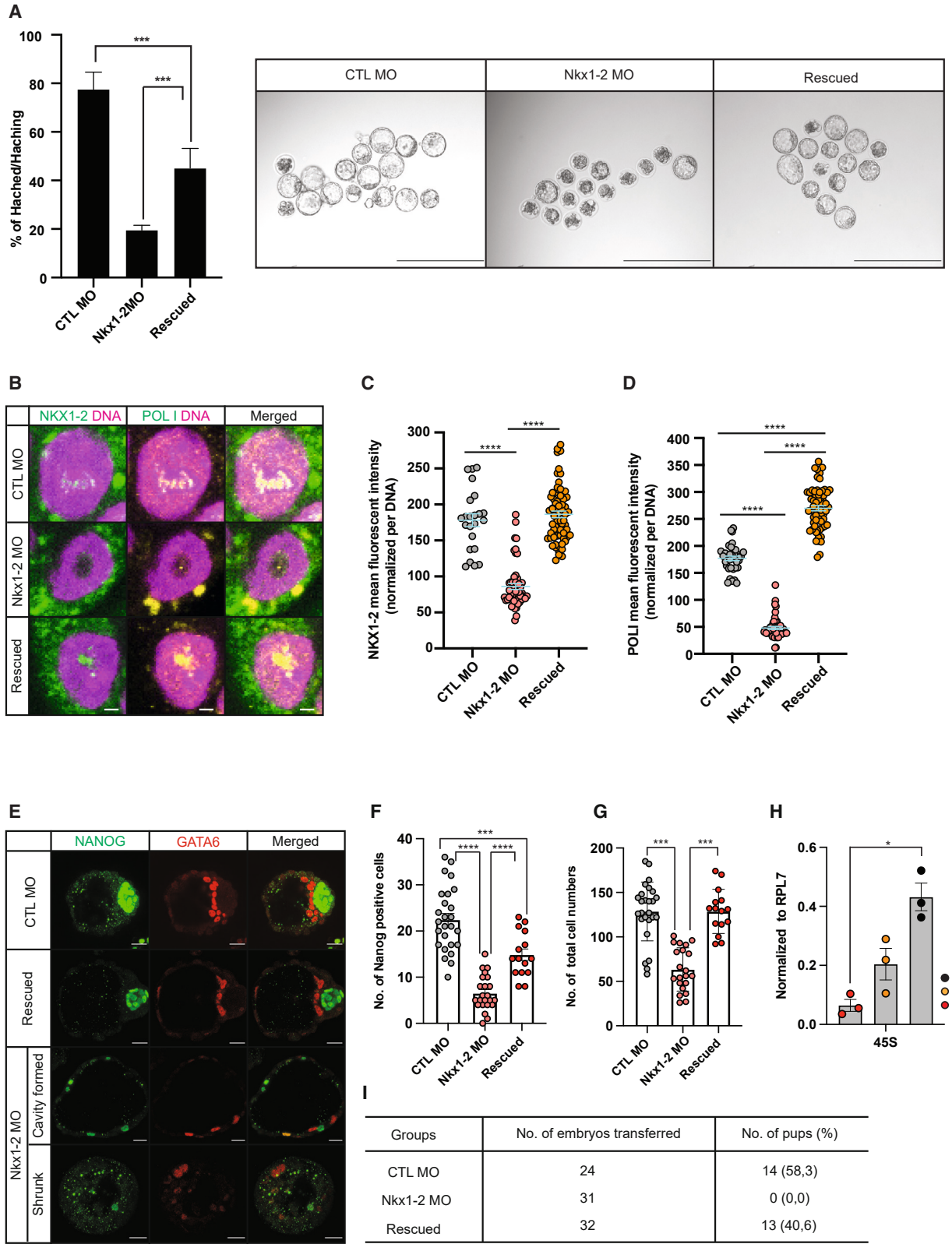

I

Groups	No. of embryos transferred	No. of pups (%)
CTL MO	24	14 (58,3)
Nkx1-2 MO	31	0 (0,0)
Rescued	32	13 (40,6)

(legend on next page)

These mechanistic regulators control the cell state via their ARACNe-inferred regulatory targets, which are used by VIPER to assess their activity. Here, MR analysis was instrumental in identifying *Nkx1-2* as a gene encoding for a novel Wnt/β-catenin-dependent factor, which we characterized to be essential for preimplantation development. We found that *Nkx1-2* encodes for a key MR controlling ribosome biogenesis, translation, mRNA processing, and the localization of POL I to nucleoli in mouse preimplantation embryos. Impairment of ribosomal function and biogenesis in *Nkx1-2* KD embryos, using either an MO-mediated or an siRNA-mediated approach, resulted in severe defects in blastomere division, homeostasis, and embryo size, culminating in the arrest of embryo development. How NKX1-2 controls embryo development still needs to be investigated; however, NKX1-2 might regulate the shuttling of POL I between the nucleoplasm to the nucleolus.

Our findings are in apparent contradiction to an earlier report that used an Nkx1-2CreER^{T2} transgenic mouse model to study the expression of *Nkx1-2* in post-implantation embryos (Rodrigo Albors et al., 2018); however, in this study, a possible isoform predicted to be encoded from an ATG (a start codon [amino acid methionine]) located before the second exon could have had some compensatory effects. Alternatively, it is possible that acute short hairpin RNA (shRNA)-mediated or MO-mediated loss of function of TFs leads to embryo developmental arrest, while compensatory mechanisms can allow viability in the KO mouse line, as it has been seen for other developmental factors (El-Brolosy et al., 2019; El-Brolosy and Stainier, 2017). Finally, besides the Wnt signaling, other pathways might regulate *Nkx1-2*, resulting in different phenotypes in KD and KO lines.

In mice, *Nkx1-2* belongs to a large homeobox gene family, the natural killer (NK) cluster, which likely stemmed from a HOX (homeobox gene HOX) cluster genome duplication and rearrangement (Larroux et al., 2007). The cluster includes 11 homeobox gene classes that encode for TFs characterized by a helix-turn-helix homeodomain, responsible for their binding to DNA (Duboule and Morata, 1994). Several studies have shown the importance of the NK gene cluster in embryo development across species. *Nkx2-5* is expressed in the heart and is essential for cardiac tissue differentiation. Indeed, *Nkx2-5*-deficient mice are embryonic lethal due to a failure in proper blood vessels and cardiac development, and mutation of the *Drosophila* ortholog *tinmon* also leads to failing of cardiac development (Tanaka et al., 1999). Thus, the function of NK genes is well conserved throughout evolution.

Nkx1-2 is expressed in the neural plate, indicating a potential role in early neural development and, specifically, in the posterior neuroectoderm specification and neuron cell fate determination (Schubert et al., 1995). Moreover, *Nkx1-2* is abundantly expressed in adult mouse brain tissue and the seminiferous epithelium in the testis (Rovescalli et al., 2000). *Nkx1-2* mRNA was detected in E7.0 mouse embryo, especially in the primitive streak (Tamashiro et al., 2012). These studies demonstrated the crucial roles of NKX1-2 in post-implantation development and morphogenesis across different species. However, the potential biological role of NKX1-2 in preimplantation development has remained elusive.

Figure 6. Preimplantation development and cell fate specification defects in *Nkx1-2* KD embryos are rescued after *Nkx1-2* mRNA injection

(A) Preimplantation development in *Nkx1-2* KD (MO-mediated) embryos was significantly improved by *Nkx1-2* mRNA injection (at E4.5). ***$p < 0.001$ (CTL-MO, $n = 116$ embryos; *Nkx1-2* KD, $n = 97$ embryos; rescued, $n = 63$ embryos). $n = 10$ independent experiments. Representative images are shown. Scale bars, 400 μm.

(B) Representative immunofluorescence images of NKX1-2 and POL I in CTL-MO, *Nkx1-2* KD, and rescued embryos. Green, NKX1-2 (anti-NKX1-2); yellow, RNA POL I (anti-RPA-194); magenta, DNA (DRAQ5). Scale bars: 5 μm.

(C) NKX1-2 mean fluorescent intensity in CTL-MO (gray; $n = 23$ blastomeres), *Nkx1-2* KD (red; $n = 54$ blastomeres), and rescued (orange; $n = 67$ blastomeres) embryos. $n = 5$ independent experiments. ****$p < 0.0001$.

(D) Mean fluorescent intensity of RNA POL I in CTL-MO (gray dots, $n = 37$ blastomeres), *Nkx1-2* KD (red dots, $n = 52$ blastomeres), and rescued (orange dots, $n = 64$ blastomeres) embryos. $n = 5$ independent experiments. ****$p < 0.0001$.

(E) Representative immunofluorescence images of NANOG (epiblast cells) and GATA6 (primitive endoderm cells) in CTL-MO, *Nkx1-2* KD (MO-mediated), and *Nkx1-2* mRNA rescued embryos (E4.5). Green, NANOG (anti-NANOG); red, GATA6 (anti-GATA6). Scale bars, 20 μm.

(F) Quantification of the number of NANOG-positive cells in CTL-MO ($n = 26$ embryos), *Nkx1-2* KD ($n = 23$ embryos), and *Nkx1-2* mRNA rescued ($n = 15$ embryos) embryos (at E4.5). $n = 4$ independent experiments. ****$p < 0.0001$, ***$p < 0.001$.

(G) Quantification of the total number of blastomeres in CTL-MO ($n = 26$ embryos), *Nkx1-2* KD ($n = 21$ embryos), and *Nkx1-2* mRNA rescued ($n = 15$ embryos) embryos (at E4.5). $n = 4$ independent experiments. ***$p < 0.001$.

(H) RT-qPCR of *45S*, in CTL, *Nkx1-2* MO, and *Nkx1-2* mRNA rescued embryos. Data are presented as mean ± SEM ($n = 3$ independent experiments; the same CTL-MO and *Nkx1-2* KD samples as used for Figure 3D were plotted). *$p = 0.0189$.

(I) CTL-MO, *Nkx1-2* KD, and rescued embryo transfer. All embryos were transferred into the uterus of a foster mother at the E3.5 stage, and pups were counted after birth. $n = 3$ independent experiments.

In the present study, we showed that *Nkx1-2* KD embryos failed to form a blastocoel and could not develop further. Our single-cell analysis showed that genes involved in controlling pre-mRNA processing, splicing, RNA nuclear export, and mRNA translation in ribosomes (such as *Hnrnpa2b1*, *Acyp1*, *Hnrnph3*) were severely downregulated in *Nkx1-2* KD embryo blastomeres. One of the most downregulated gene, *Hnrnpa2b1*, is essential for preimplantation development and cell fate specification in mouse (Kwon et al., 2019). Indeed, *Hnrnpa2b1* KD mouse embryos also showed a blastocoel formation defect comparable to what we observed in this study. HNRNPA2B1 is regulated by methyltransferase-like 3 (METTL3)-dependent m^6A RNA methylation (Alarcon et al., 2015; Kwon et al., 2019; Liu et al., 2014). It has recently been reported that METTL3 regulates heterochromatin formation in mESCs (Xu et al., 2021), which is in agreement with our observation that NKX1-2 localizes inside and at the periphery of the nucleoli of oocytes and preimplantation embryos. Therefore, it would be interesting in the future to investigate the role of NKX1-2 in heterochromatin formation.

We showed that NKX1-2 colocalized with UBTF, which regulates the transcription of ribosomal genes (Hamdane et al., 2014; Kone et al., 2016) and is also a co-factor of POL I (Hamdane et al., 2014; Kwon and Green, 1994). In fully grown GV oocytes that have no transcription activity (Borsos and Torres-Padilla, 2016; Inoue et al., 2008), NKX1-2 and UBTF form large, non-overlapping clusters. However, both NKX1-2 and UBTF co-localize and spread throughout the nucleolus in the developing embryos as well as in the growing GV oocytes, in which transcription is very active (Borsos and Torres-Padilla, 2016; Inoue et al., 2008). These results suggest that NKX1-2 as well as UBTF (Hamdane et al., 2014) might cooperate in the control of ribosomal transcriptional activity. Components of the POL I holoenzyme are exchanged rapidly between the nucleoplasm and the nucleolus, where the holoenzyme is assembled to transcribe ribosomal genes (Dundr et al., 2002; Grummt, 2003). Nascent RNA synthesis, rRNAs, and POL I nucleolar localization were dramatically altered in *Nkx1-2* KD embryos, suggesting a key role of NKX1-2 in ribosomal function. We also showed that expression of the pre-ribosomal RNA gene *45S* was significantly decreased in *Nkx1-2* KD embryos. However, we did not see a significant reduction of other rRNA genes, such as for *18S* and *28S* rRNAs. We cannot exclude that the RT-qPCR results were limited by the low cDNA levels and that using a much larger number of preimplantation embryos could show significant differences also for *18S* and *28S* rRNA expression. Indeed, the structure of nucleoli was severely altered in *Nkx1-2* KD embryos, as shown in TEM experiments.

The ribosomal activity alteration was likely the cause of chromosome segregation defects already at 2- and 4-cell stages, as well as of the consequent preimplantation development arrest. The precise role of nucleolar proteins during cell division is still elusive. Some nucleolar proteins relocate to the chromosome periphery during mitosis and are required for proper spindle formation and chromosome alignment (Ma et al., 2007; Stenstrom et al., 2020). NKX1-2 localizes in the nucleoli of oocytes and embryos but also at the centromeres of mitotic chromosomes in the metaphase blastomeres. Live-cell imaging showed severe cell division defects, including binucleation and lagging chromosomes, in *Nkx1-2* KD embryos during preimplantation development. This was coupled with disorganized MTs and multipolar spindle formation. It is well known that multipolar spindle formation is sufficient to induce merotelic K-MT attachment (Nakagawa and FitzHarris, 2017; Thompson and Compton, 2011), in which a single kinetochore simultaneously attaches to MTs from both spindle poles, and that merotelic K-MT attachment leads to lagging chromosomes, micronucleus formation, and aneuploidy (Bakhoum et al., 2009; Cimini et al., 2001). The chaotic MT nucleation observed in *Nkx1-2* KD embryos is likely the cause of multipolar spindle formation, merotelic K-MT attachment, lagging chromosomes, and chromosome division errors. Further investigation is needed to unravel whether the reduced translation of a specific factor in *Nkx1-2* KD cells is responsible for the altered MT nucleation and chromosome segregation observed during preimplantation development.

Blastocoel formation is a critical step for cell fate specification during preimplantation development (Chan and Hiiragi, 2020; Ryan et al., 2019). The emergence of a blastocoel starts from the accumulation of solutes in the intercellular space (Chan and Hiiragi, 2020), prompted by the influx of fluid via ion channels or aquaporins (Navis and Bagnat, 2015). Actomyosin contractility and cell-to-cell adhesion have critical roles in fluid-filled lumina formation in epithelial and endothelial cells (Hannezo and Heisenberg, 2019; Lecuit et al., 2011; Munjal and Lecuit, 2014) and in mouse embryos (Dumortier et al., 2019; Samarage et al., 2015). The blastocoel expansion triggers Epi-PrE cell fate specification in the ICM of mouse embryos (Chan et al., 2019; Ryan et al., 2019). Indeed, if a blastocoel is deflated by using inhibitors or inserting a micro-needle in the cavity, lineage specification of the ICM is impaired (Chan et al., 2019; Chan and Hiiragi, 2020; Ryan et al., 2019). We observed that, while the timing of blastocoel formation was not altered in *Nkx1-2* KD embryos, they failed to increase volume even after 6 cycles of blastocoel increasing/collapsing. Sealing of the TJ at the cell-to-cell contact sites is one of the essential events for blastocoel expansion (Chan et al., 2019), and proper TJ protein expression is also critical for TJ sealing (Chan et al., 2019; Eckert and Fleming, 2008; Wang et al., 2008). We observed

a dramatically reduced expression of the TJ proteins and aberrant expression of actomyosin in *Nkx1-2* KD embryos, indicating that these defects trigger the failure of TJ sealing and the consequent impairment of blastocoel expansion, finally leading to cell fate specification impairment.

In sum, using an unbiased systems biology approach, we identified NKX1-2 as a novel Wnt/β-catenin-dependent MR that is essential for preimplantation development and cell fate specification via its role in ribosomal biogenesis and Pol I activity in the mouse embryo.

EXPERIMENTAL PROCEDURES

Resource availability

All data are available in the main text or the supplementary materials. Additional materials generated in this study are available from the corresponding author upon request.

Lead contact

Further information and requests for resources and reagents should be directed to and will be fulfilled by the corresponding author Maria Pia Cosma: pia.cosma@crg.es.

Materials availability

No new reagents were generated for this report.

Data and code availability

RNA-seq dataset has been deposited at the NCBI GEO repository under access code GSE202079.

Oocyte and embryo collection

Growing and fully grown GV oocytes and zygotes were collected from 4- to 12-week-old C57B6F1 (BDF1) females and from 6- to 12-week-old superovulated C57B6F1 (BDF1) females mated with BDF1 males (Charles River Laboratories), respectively. Details on protocols and culturing conditions are specified in the supplementary material.

Microinjection

mRNAs were manufactured using Ambion mMessage mMachine kit according to manufacturer's instructions. Antisense MOs were purchased from Gene Tools and diluted to 1.0 mM with sterile water. MO sequences were as follows.

Nkx1-2 MO, 5′-CGTCCTGCCATGCCAACATG-3′

CTL-MO 5′-TCCAGGTCCCCCGCATCCCGGATCC-3′

We used translation-blocking MOs that target the 5′ UTR through the first 25 bases of coding sequence. Stealth siRNAs (see sequences in the following) were purchased from Invitrogen and diluted to 20 μM with RNase-free water. CTL-siRNA was purchased from Invitrogen.

Nkx1-2 siRNA#1, 5′-CCCUCUCACCACAAGAUCUCCUUCU-3′

Nkx1-2 siRNA#2, 5′-AGAAGAGGUGGAAGCAGGGCAAGAU-3′

MO, siRNA, or mRNA were microinjected into zygote cytoplasm using Narishige micromanipulators mounted on an Olympus inverted microscope.

Immunofluorescence and imaging

Oocytes and embryos were fixed with 2% paraformaldehyde (PFA) (Alfa Aesar, #43368), in PBS for 10 min and permeabilization with 0.25% Triton X-100 (Sigma-Aldrich, #T8787-100 mL) for 10 min. Blocking was performed with 3% bovine serum albumin (BSA) (Sigma-Aldrich, #A7906-100G) for 1 h at 37°C or overnight at 4°C. See supplementary material for the primary and secondary antibodies and imaging conditions.

mESC context-specific interactome

The transcriptome of 208 independent samples from two mESC strains (JM8.N4 and R1) were profiled by RNA-seq, following perturbations with a combination of small molecules and morphogens aimed at modulating the activity of regulatory and signaling genes for interactome reverse engineering purposes. Specifically, mESCs were maintained feeder free in N2B27 medium supplemented with 1 μM PD184352 (Biovision, Cat#1585-5), 3 μM CHIR99021 (Sigma-Aldrich, Cat#A3734), and 2 μM SU5402 (Tocris Bioscience, Cat#3300) as described previously (Ying et al., 2008). To generate samples for interactome reverse engineering, both strains were incubated for 24 h with N2B27 medium supplemented with one of four differentiation morphogens—20 ng/mL activin A (Gemini Bio-Products, #300356), 6 ng/mL bFGF (Basic Fibroblast Growth Factor) (Gemini Bio-Products, #300305), 2 ng/mL BMP4 (Gemini Bio-Products, #300236P), or 5 μM retinoic acid (Sigma-Aldrich, #R2625)—or in N2B27 medium alone, followed by a 30-h incubation in N2B27 medium supplemented with one of 24 perturbagens (see Table S1). RNA was then extracted using TRIzol (Thermo Fisher Scientific, #15596018) following the manufacturer's instructions, and RNA was stored in RNA-free water at −80°C until RNA-seq was performed. RNA-seq data were generated according to the polyA-capture Illumina TruSeq protocol in a HiSeq 2000 instrument (Illumina) at the Columbia Sulzberger Genome Center. Sequencing data were mapped to the mouse genome MGSCv37 (mm9) with TopHat2 (Kim et al., 2013). Reads that mapped to known genes, based on Entrez gene identifiers, were counted using the GenomicFeatures R-system package available from Bioconductor (Gentleman et al., 2004). Summarized expression data resulting from these analyses, available from the Gene Expression Omnibus database (GSE202079), consist of a raw-counts expression matrix of 21,761 known genes by 208 samples. Expression data were normalized by equivariance transformation based on negative binomial distribution, using the DESeq R-system package (Anders and Huber, 2010). The transcriptional interactome was reverse engineered by the ARACNe algorithm (Basso et al., 2005; Margolin et al., 2006), using 1,490 genes annotated as TFs in the GO Molecular Function database (specifically, as GO:0003700, *transcription factor activity*; GO:0004677, *DNA binding*; GO:0030528, *transcription regulator activity*; GO:0004677, *DNA-dependent protein kinase activity*; or GO:0045449, *regulation of transcription*) as potential regulators, and 100 bootstrap iterations were performed. Parameters were set to a data processing inequality (DPI) of 0 tolerance and an MI (mutual information) *p*-value threshold of 10^{-8}. The resulting interactome represents a regulatory map between 1,490 TFs and 18,748 target genes, through 754,361 transcriptional interactions. A network model for the mESC context-specific transcriptional regulation (interactome) was assembled based on the ARACNe-inferred interactions between TFs and target transcripts, and the mode of regulation inferred by correlation analysis as previously described (Alvarez et al., 2016) (see Table S2).

Protein activity inference by VIPER

The protein activity of each TF represented in the mESCs was inferred using the VIPER algorithm (Alvarez et al., 2016), using multi-sample (ms)VIPER to deal with the six replicate samples for

each mutant cell line. The normalized and batch effect-corrected gene expression profiles of each mutant cell line were subjected to a gene-wise Student's t test against the WT gene expression profiles to generate a gene expression signature. To maximize the robustness of the analysis, n = 1,000 null model gene expression signatures were also generated by shuffling the samples between the WT and mutant groups. For each TF, the top 200 target genes were considered (based on p values from the mESC interactome). An enrichment score was computed based on the target gene enrichment for each TF from the mutant/null gene expression signature. The protein activity of each TF was then measured as the normalized enrichment score by comparing the mutant enrichment scores to the distribution of all the null enrichment scores.

Embryo transfer

Seven to ten CTL-MO, *Nkx1-2* KD, or rescued embryos at E3.5 were transferred into CD1 pseudo-pregnant females (at 2.5 days after copulation with vasectomized males). Pups were counted at birth.

Image analysis and statistics

All image processing and analyses were performed using ImageJ/Fiji (https://imageJ.net/download/). Signal intensity (SI) of NKX1-2 in Figure 2G was quantified using the 3D Objects Counter plugin on Fiji. The mean SI and surface areas were measured from the object maps based on the recognized NKX1-2 signals (from the 3D Objects Counter). The mean SI of EU for Figure 3C was normalized by DNA SI. To quantify the SI of E-cadherin and F-actin in Figure 5F, a free-hand line was drawn along the cell-to-cell junctions, and the mean gray values were measured. All data were analyzed by GraphPad Prism 9 software (GraphPad Software, La Jolla, CA, USA), and significance was calculated using one-way ANOVA and Tukey's multiple comparisons test. Statistical significance was considered if $p < 0.05$.

SUPPLEMENTAL INFORMATION

Supplemental information can be found online at https://doi.org/10.1016/j.stemcr.2024.04.004.

ACKNOWLEDGMENTS

We would like to thank the PRBB animal facility and the CRG core techologies programme, the CRG Advanced Microscopy Unit (PRBB, Barcelona, Spain) and the IDIBELL Scientific and Technical Services for the electron microscopy experiments and image analysis (IDIBELL, Barcelona, Spain). We would like to thank Carlotta Viana for the cover art. This work was supported by the Ministerio de Ciencia e Innovación, (BFU2017-86760-P (AEI/FEDER, UE) and PID2020-114080GB-I00 / AEI/10.13039/501100011033 to M.P.C.), the AGAUR grant from Secretaria d'Universitats i Recerca del Departament d'Empresa i Coneixement de la Generalitat de Catalunya, (2017 SGR 689 and 2021-SGR2021-01300 to M.P.C.), the Fundacio La Marato de TV3, (202027-10 to M.P.C.), the NSFC (32270577 to M.P.C.), the European Union's Horizon 2020 research and innovation program under grant agreement Nº964342 to M.P.C., from "La Caixa" Foundation (HR17-00231 to M.P.C.), NCI Outstanding Investigator award (R35 CA 197745 to A.C.), NIH Shared Instrumentation Grants (S10 OD012351, S10 OD021764, and S10OD032433, all to A.C.), NIH R01 (HD085904 and CA238005 to M.M.S), FI-AGAUR PhD fellowship from the Secretaria d'Universitats i Recerca del Departament d'Empresa i Coneixement de la Generalitat de Catalunya and the co-finance of Fondo Social Europeo (2018FI_B_00637 and FSE to R.S.-P.), the Ramon y Cajal program of the Ministerio de Ciencia, Innovación y Universidades, and the European Social Fund (RYC-2018-025002-I to S.A.), and the Instituto de Salud Carlos III-FEDER (PI19/01814 to S.A.). We acknowledge support of the Spanish Ministry of Science and Innovation through the Centro de Excelencia Severo Ochoa (CEX2020-001049-S, MCIN/AEI/10.13039/501100011033), and the CERCA Programme/Generalitat de Catalunya.

AUTHOR CONTRIBUTIONS

S.N. and M.P.C. conceptualized this work. S.N. designed and performed all the experiments reported in Figures 2, 3, 4, 5, 6, and S3. D.C., X.T., M.J.A., D.-E.P., K.A., and W.S. performed computational analyses reported in Figures 1, 2, S1, and S2. S.N. and D.N. conducted the live-cell imaging reported in Figure 4. Data were primarily analyzed by S.N. with contributions from U.D.V., X.T., M.J.A., D.-E.P., U.D.V., K.A., W.S., S.A., D.N., R.S.-P., C.C., P.C, and M.V.N. S.N., D.C., X.T., M.J.A., K.A., D.N., R.S.-P., M.V.N., and M.P.C. wrote the manuscript. M.J.A., D.-E.P. and M.M.S. built the mouse ESC interactome reported in Tables S1 and S2. A.C. and M.P.C. supervised the project.

DECLARATION OF INTERESTS

A.C. is founder, equity holder, and consultant, and M.J.A. is Chief Scientific Officer at DarwinHealth Inc., a company that has licensed some of the algorithms used in this manuscript from Columbia University. Columbia University is also an equity holder in DarwinHealth Inc.

Received: June 23, 2022
Revised: April 4, 2024
Accepted: April 5, 2024
Published: May 2, 2024

REFERENCES

Alarcón, C.R., Goodarzi, H., Lee, H., Liu, X., Tavazoie, S., and Tavazoie, S.F. (2015). HNRNPA2B1 Is a Mediator of m(6)A-Dependent Nuclear RNA Processing Events. Cell *162*, 1299–1308. https://doi.org/10.1016/j.cell.2015.08.011.

Alvarez, M.J., Shen, Y., Giorgi, F.M., Lachmann, A., Ding, B.B., Ye, B.H., and Califano, A. (2016). Functional characterization of somatic mutations in cancer using network-based inference of protein activity. Nat. Genet. *48*, 838–847. https://doi.org/10.1038/ng.3593.

Anders, S., and Huber, W. (2010). Differential expression analysis for sequence count data. Genome Biol. *11*, R106. https://doi.org/10.1186/gb-2010-11-10-r106.

Arroyo, M., and Trepat, X. (2019). Embryonic self-fracking. Science *365*, 442–443. https://doi.org/10.1126/science.aay2860.

Aulicino, F., Pedone, E., Sottile, F., Lluis, F., Marucci, L., and Cosma, M.P. (2020). Canonical Wnt Pathway Controls mESC Self-Renewal Through Inhibition of Spontaneous Differentiation via

beta-Catenin/TCF/LEF Functions. Stem Cell Rep. *15*, 646–661. https://doi.org/10.1016/j.stemcr.2020.07.019.

Bader, G.D., and Hogue, C.W.V. (2003). An automated method for finding molecular complexes in large protein interaction networks. BMC Bioinf. *4*, 2. https://doi.org/10.1186/1471-2105-4-2.

Bakhoum, S.F., Genovese, G., and Compton, D.A. (2009). Deviant kinetochore microtubule dynamics underlie chromosomal instability. Curr. Biol. *19*, 1937–1942. https://doi.org/10.1016/j.cub.2009.09.055.

Basso, K., Margolin, A.A., Stolovitzky, G., Klein, U., Dalla-Favera, R., and Califano, A. (2005). Reverse engineering of regulatory networks in human B cells. Nat. Genet. *37*, 382–390. https://doi.org/10.1038/ng1532.

Boisvert, F.M., van Koningsbruggen, S., Navascués, J., and Lamond, A.I. (2007). The multifunctional nucleolus. Nat. Rev. Mol. Cell Biol. *8*, 574–585. https://doi.org/10.1038/nrm2184.

Boroviak, T., Loos, R., Lombard, P., Okahara, J., Behr, R., Sasaki, E., Nichols, J., Smith, A., and Bertone, P. (2015). Lineage-Specific Profiling Delineates the Emergence and Progression ofIe Pluripotency in Mammalian Embryogenesis. Dev. Cell *35*, 366–382. https://doi.org/10.1016/j.devcel.2015.10.011.

Borsos, M., and Torres-Padilla, M.E. (2016). Building up the nucleus: nuclear organization in the establishment of totipotency and pluripotency during mammalian development. Genes Dev. *30*, 611–621. https://doi.org/10.1101/gad.273805.115.

Chan, C.J., Costanzo, M., Ruiz-Herrero, T., Mönke, G., Petrie, R.J., Bergert, M., Diz-Muñoz, A., Mahadevan, L., and Hiiragi, T. (2019). Hydraulic control of mammalian embryo size and cell fate. Nature *571*, 112–116. https://doi.org/10.1038/s41586-019-1309-x.

Chan, C.J., and Hiiragi, T. (2020). Integration of luminal pressure and signalling in tissue self-organization. Development *147*, dev181297. https://doi.org/10.1242/dev.181297.

Cimini, D., Howell, B., Maddox, P., Khodjakov, A., Degrassi, F., and Salmon, E.D. (2001). Merotelic kinetochore orientation is a major mechanism of aneuploidy in mitotic mammalian tissue cells. J. Cell Biol. *153*, 517–527. https://doi.org/10.1083/jcb.153.3.517.

Duboule, D., and Morata, G. (1994). Colinearity and functional hierarchy among genes of the homeotic complexes. Trends Genet. *10*, 358–364. https://doi.org/10.1016/0168-9525(94)90132-5.

Dumortier, J.G., Le Verge-Serandour, M., Tortorelli, A.F., Mielke, A., de Plater, L., Turlier, H., and Maître, J.L. (2019). Hydraulic fracturing and active coarsening position the lumen of the mouse blastocyst. Science *365*, 465–468. https://doi.org/10.1126/science.aaw7709.

Dundr, M., Hoffmann-Rohrer, U., Hu, Q., Grummt, I., Rothblum, L.I., Phair, R.D., and Misteli, T. (2002). A kinetic framework for a mammalian RNA polymerase in vivo. Science *298*, 1623–1626. https://doi.org/10.1126/science.1076164.

Eckersley-Maslin, M.A., Alda-Catalinas, C., and Reik, W. (2018). Dynamics of the epigenetic landscape during the maternal-to-zygotic transition. Nat. Rev. Mol. Cell Biol. *19*, 436–450. https://doi.org/10.1038/s41580-018-0008-z.

Eckert, J.J., and Fleming, T.P. (2008). Tight junction biogenesis during early development. Biochim. Biophys. Acta *1778*, 717–728. https://doi.org/10.1016/j.bbamem.2007.09.031.

El-Brolosy, M.A., Kontarakis, Z., Rossi, A., Kuenne, C., Günther, S., Fukuda, N., Kikhi, K., Boezio, G.L.M., Takacs, C.M., Lai, S.L., et al. (2019). Genetic compensation triggered by mutant mRNA degradation. Nature *568*, 193–197. https://doi.org/10.1038/s41586-019-1064-z.

El-Brolosy, M.A., and Stainier, D.Y.R. (2017). Genetic compensation: A phenomenon in search of mechanisms. PLoS Genet. *13*, e1006780. https://doi.org/10.1371/journal.pgen.1006780.

Fenech, M., Kirsch-Volders, M., Natarajan, A.T., Surralles, J., Crott, J.W., Parry, J., Norppa, H., Eastmond, D.A., Tucker, J.D., and Thomas, P. (2011). Molecular mechanisms of micronucleus, nucleoplasmic bridge and nuclear bud formation in mammalian and human cells. Mutagenesis *26*, 125–132. https://doi.org/10.1093/mutage/geq052.

Fulka, H., and Aoki, F. (2016). Nucleolus Precursor Bodies and Ribosome Biogenesis in Early Mammalian Embryos: Old Theories and New Discoveries. Biol. Reprod. *94*, 143. https://doi.org/10.1095/biolreprod.115.136093.

Gentleman, R.C., Carey, V.J., Bates, D.M., Bolstad, B., Dettling, M., Dudoit, S., Ellis, B., Gautier, L., Ge, Y., Gentry, J., et al. (2004). Bioconductor: open software development for computational biology and bioinformatics. Genome Biol. *5*, R80. https://doi.org/10.1186/gb-2004-5-10-r80.

Grummt, I. (2003). Life on a planet of its own: regulation of RNA polymerase I transcription in the nucleolus. Genes Dev. *17*, 1691–1702. https://doi.org/10.1101/gad.1098503R.

Haegel, H., Larue, L., Ohsugi, M., Fedorov, L., Herrenknecht, K., and Kemler, R. (1995). Lack of beta-catenin affects mouse development at gastrulation. Development *121*, 3529–3537. https://doi.org/10.1242/dev.121.11.3529.

Hamdane, N., Stefanovsky, V.Y., Tremblay, M.G., Németh, A., Paquet, E., Lessard, F., Sanij, E., Hannan, R., and Moss, T. (2014). Conditional inactivation of Upstream Binding Factor reveals its epigenetic functions and the existence of a somatic nucleolar precursor body. PLoS Genet. *10*, e1004505. https://doi.org/10.1371/journal.pgen.1004505.

Hannezo, E., and Heisenberg, C.P. (2019). Mechanochemical Feedback Loops in Development and Disease. Cell *178*, 12–25. https://doi.org/10.1016/j.cell.2019.05.052.

Hassold, T., and Hunt, P. (2001). To err (meiotically) is human: the genesis of human aneuploidy. Nat. Rev. Genet. *2*, 280–291. https://doi.org/10.1038/35066065.

Huelsken, J., Vogel, R., Brinkmann, V., Erdmann, B., Birchmeier, C., and Birchmeier, W. (2000). Requirement for beta-catenin in anterior-posterior axis formation in mice. J. Cell Biol. *148*, 567–578. https://doi.org/10.1083/jcb.148.3.567.

Inoue, A., Nakajima, R., Nagata, M., and Aoki, F. (2008). Contribution of the oocyte nucleus and cytoplasm to the determination of meiotic and developmental competence in mice. Hum. Reprod. *23*, 1377–1384. https://doi.org/10.1093/humrep/den096.

Kemp, C., Willems, E., Abdo, S., Lambiv, L., and Leyns, L. (2005). Expression of all Wnt genes and their secreted antagonists during mouse blastocyst and postimplantation development. Dev. Dynam. *233*, 1064–1075. https://doi.org/10.1002/dvdy.20408.

Kim, D., Pertea, G., Trapnell, C., Pimentel, H., Kelley, R., and Salzberg, S.L. (2013). TopHat2: accurate alignment of transcriptomes in the presence of insertions, deletions and gene fusions. Genome Biol. *14*, R36. https://doi.org/10.1186/gb-2013-14-4-r36.

Kishimoto, K., Furukawa, K.T., Luz-Madrigal, A., Yamaoka, A., Matsuoka, C., Habu, M., Alev, C., Zorn, A.M., and Morimoto, M. (2020). Bidirectional Wnt signaling between endoderm and mesoderm confers tracheal identity in mouse and human cells. Nat. Commun. *11*, 4159. https://doi.org/10.1038/s41467-020-17969-w.

Koné, M.C., Fleurot, R., Chebrout, M., Debey, P., Beaujean, N., and Bonnet-Garnier, A. (2016). Three-Dimensional Distribution of UBF and Nopp140 in Relationship to Ribosomal DNA Transcription During Mouse Preimplantation Development. Biol. Reprod. *94*, 95. https://doi.org/10.1095/biolreprod.115.136366.

Kwon, H., and Green, M.R. (1994). The RNA polymerase I transcription factor, upstream binding factor, interacts directly with the TATA box-binding protein. J. Biol. Chem. *269*, 30140–30146.

Kwon, J., Jo, Y.J., Namgoong, S., and Kim, N.H. (2019). Functional roles of hnRNPA2/B1 regulated by METTL3 in mammalian embryonic development. Sci. Rep. *9*, 8640. https://doi.org/10.1038/s41598-019-44714-1.

Larroux, C., Fahey, B., Degnan, S.M., Adamski, M., Rokhsar, D.S., and Degnan, B.M. (2007). The NK homeobox gene cluster predates the origin of Hox genes. Curr. Biol. *17*, 706–710. https://doi.org/10.1016/j.cub.2007.03.008.

Lecuit, T., Lenne, P.F., and Munro, E. (2011). Force generation, transmission, and integration during cell and tissue morphogenesis. Annu. Rev. Cell Dev. Biol. *27*, 157–184. https://doi.org/10.1146/annurev-cellbio-100109-104027.

Lefebvre, C., Rajbhandari, P., Alvarez, M.J., Bandaru, P., Lim, W.K., Sato, M., Wang, K., Sumazin, P., Kustagi, M., Bisikirska, B.C., et al. (2010). A human B-cell interactome identifies MYB and FOXM1 as master regulators of proliferation in germinal centers. Mol. Syst. Biol. *6*, 377. https://doi.org/10.1038/msb.2010.31.

Lindström, M.S., Bartek, J., and Maya-Mendoza, A. (2022). p53 at the crossroad of DNA replication and ribosome biogenesis stress pathways. Cell Death Differ. *29*, 972–982. https://doi.org/10.1038/s41418-022-00999-w.

Liu, J., Yue, Y., Han, D., Wang, X., Fu, Y., Zhang, L., Jia, G., Yu, M., Lu, Z., Deng, X., et al. (2014). A METTL3-METTL14 complex mediates mammalian nuclear RNA N6-adenosine methylation. Nat. Chem. Biol. *10*, 93–95. https://doi.org/10.1038/nchembio.1432.

Liu, T.Y., Chen, Y.C., Jong, Y.J., Tsai, H.J., Lee, C.C., Chang, Y.S., Chang, J.G., and Chang, Y.F. (2017). Muscle developmental defects in heterogeneous nuclear Ribonucleoprotein A1 knockout mice. Open Biol. *7*, 160303. https://doi.org/10.1098/rsob.160303.

Lluis, F., Ombrato, L., Pedone, E., Pepe, S., Merrill, B.J., and Cosma, M.P. (2011). T-cell factor 3 (Tcf3) deletion increases somatic cell reprogramming by inducing epigenome modifications. Proc. Natl. Acad. Sci. USA *108*, 11912–11917. https://doi.org/10.1073/pnas.1017402108.

Ma, N., Matsunaga, S., Takata, H., Ono-Maniwa, R., Uchiyama, S., and Fukui, K. (2007). Nucleolin functions in nucleolus formation and chromosome congression. J. Cell Sci. *120*, 2091–2105. https://doi.org/10.1242/jcs.008771.

Maître, J.L., Niwayama, R., Turlier, H., Nédélec, F., and Hiiragi, T. (2015). Pulsatile cell-autonomous contractility drives compaction in the mouse embryo. Nat. Cell Biol. *17*, 849–855. https://doi.org/10.1038/ncb3185.

Margolin, A.A., Nemenman, I., Basso, K., Wiggins, C., Stolovitzky, G., Dalla Favera, R., and Califano, A. (2006). ARACNE: an algorithm for the reconstruction of gene regulatory networks in a mammalian cellular context. BMC Bioinf. *7*, S7. https://doi.org/10.1186/1471-2105-7-S1-S7.

Merrill, B.J. (2012). Wnt pathway regulation of embryonic stem cell self-renewal. Cold Spring Harbor Perspect. Biol. *4*, a007971. https://doi.org/10.1101/cshperspect.a007971.

Munjal, A., and Lecuit, T. (2014). Actomyosin networks and tissue morphogenesis. Development *141*, 1789–1793. https://doi.org/10.1242/dev.091645.

Muñoz-Descalzo, S., Hadjantonakis, A.K., and Arias, A.M. (2015). Wnt/ss-catenin signalling and the dynamics of fate decisions in early mouse embryos and embryonic stem (ES) cells. Semin. Cell Dev. Biol. *47–48*, 101–109. https://doi.org/10.1016/j.semcdb.2015.08.011.

Nakagawa, S., and FitzHarris, G. (2017). Intrinsically Defective Microtubule Dynamics Contribute to Age-Related Chromosome Segregation Errors in Mouse Oocyte Meiosis-I. Curr. Biol. *27*, 1040–1047. https://doi.org/10.1016/j.cub.2017.02.025.

Navis, A., and Bagnat, M. (2015). Developing pressures: fluid forces driving morphogenesis. Curr. Opin. Genet. Dev. *32*, 24–30. https://doi.org/10.1016/j.gde.2015.01.010.

Obradovic, A., Chowdhury, N., Haake, S.M., Ager, C., Wang, V., Vlahos, L., Guo, X.V., Aggen, D.H., Rathmell, W.K., Jonasch, E., et al. (2021). Single-cell protein activity analysis identifies recurrence-associated renal tumor macrophages. Cell *184*, 2988–3005.e16. https://doi.org/10.1016/j.cell.2021.04.038.

Paull, E.O., Aytes, A., Jones, S.J., Subramaniam, P.S., Giorgi, F.M., Douglass, E.F., Tagore, S., Chu, B., Vasciaveo, A., Zheng, S., et al. (2021). A modular master regulator landscape controls cancer transcriptional identity. Cell *184*, 334–351.e20. https://doi.org/10.1016/j.cell.2020.11.045.

Rodrigo Albors, A., Halley, P.A., and Storey, K.G. (2018). Lineage tracing of axial progenitors using Nkx1-2CreER(T2) mice defines their trunk and tail contributions. Development *145*, dev164319. https://doi.org/10.1242/dev.164319.

Rovescalli, A.C., Cinquanta, M., Ferrante, J., Kozak, C.A., and Nirenberg, M. (2000). The mouse Nkx-1.2 homeobox gene: alternative RNA splicing at canonical and noncanonical splice sites. Proc. Natl. Acad. Sci. USA *97*, 1982–1987. https://doi.org/10.1073/pnas.030539397.

Ryan, A.Q., Chan, C.J., Graner, F., and Hiiragi, T. (2019). Lumen Expansion Facilitates Epiblast-Primitive Endoderm Fate Specification during Mouse Blastocyst Formation. Dev. Cell *51*, 684–697.e4. https://doi.org/10.1016/j.devcel.2019.10.011.

Samarage, C.R., White, M.D., Álvarez, Y.D., Fierro-González, J.C., Henon, Y., Jesudason, E.C., Bissiere, S., Fouras, A., and Plachta, N. (2015). Cortical Tension Allocates the First Inner Cells of the Mammalian Embryo. Dev. Cell *34*, 435–447. https://doi.org/10.1016/j.devcel.2015.07.004.

Schubert, F.R., Fainsod, A., Gruenbaum, Y., and Gruss, P. (1995). Expression of the novel murine homeobox gene Sax-1 in the developing nervous system. Mech. Dev. *51*, 99–114. https://doi.org/10.1016/0925-4773(95)00358-8.

Stenström, L., Mahdessian, D., Gnann, C., Cesnik, A.J., Ouyang, W., Leonetti, M.D., Uhlén, M., Cuylen-Haering, S., Thul, P.J., and Lundberg, E. (2020). Mapping the nucleolar proteome reveals a spatiotemporal organization related to intrinsic protein disorder. Mol. Syst. Biol. *16*, e9469. https://doi.org/10.15252/msb.20209469.

Tamashiro, D.A.A., Alarcon, V.B., and Marikawa, Y. (2012). Nkx1-2 is a transcriptional repressor and is essential for the activation of Brachyury in P19 mouse embryonal carcinoma cell. Differentiation. *83*, 282–292. https://doi.org/10.1016/j.diff.2012.02.010.

Tanaka, M., Chen, Z., Bartunkova, S., Yamasaki, N., and Izumo, S. (1999). The cardiac homeobox gene Csx/Nkx2.5 lies genetically upstream of multiple genes essential for heart development. Development *126*, 1269–1280. https://doi.org/10.1242/dev.126.6.1269.

ten Berge, D., Koole, W., Fuerer, C., Fish, M., Eroglu, E., and Nusse, R. (2008). Wnt signaling mediates self-organization and axis formation in embryoid bodies. Cell Stem Cell *3*, 508–518. https://doi.org/10.1016/j.stem.2008.09.013.

ten Berge, D., Kurek, D., Blauwkamp, T., Koole, W., Maas, A., Eroglu, E., Siu, R.K., and Nusse, R. (2011). Embryonic stem cells require Wnt proteins to prevent differentiation to epiblast stem cells. Nat. Cell Biol. *13*, 1070–1075. https://doi.org/10.1038/ncb2314.

Theka, I., Sottile, F., Cammisa, M., Bonnin, S., Sanchez-Delgado, M., Di Vicino, U., Neguembor, M.V., Arumugam, K., Aulicino, F., Monk, D., et al. (2019). Wnt/beta-catenin signaling pathway safeguards epigenetic stability and homeostasis of mouse embryonic stem cells. Sci. Rep. *9*, 948. https://doi.org/10.1038/s41598-018-37442-5.

Thompson, S.L., and Compton, D.A. (2011). Chromosome missegregation in human cells arises through specific types of kinetochore-microtubule attachment errors. Proc. Natl. Acad. Sci. USA *108*, 17974–17978. https://doi.org/10.1073/pnas.1109720108.

Tsukita, S., Furuse, M., and Itoh, M. (2001). Multifunctional strands in tight junctions. Nat. Rev. Mol. Cell Biol. *2*, 285–293. https://doi.org/10.1038/35067088.

Vautier, D., Chesné, P., Cunha, C., Calado, A., Renard, J.P., and Carmo-Fonseca, M. (2001). Transcription-dependent nucleocytoplasmic distribution of hnRNP A1 protein in early mouse embryos. J. Cell Sci. *114*, 1521–1531. https://doi.org/10.1242/jcs.114.8.1521.

Wang, B., Pfeiffer, M.J., Schwarzer, C., Araúzo-Bravo, M.J., and Boiani, M. (2014). DNA replication is an integral part of the mouse oocyte's reprogramming machinery. PLoS One *9*, e97199. https://doi.org/10.1371/journal.pone.0097199.

Wang, H., Ding, T., Brown, N., Yamamoto, Y., Prince, L.S., Reese, J., and Paria, B.C. (2008). Zonula occludens-1 (ZO-1) is involved in morula to blastocyst transformation in the mouse. Dev. Biol. *318*, 112–125. https://doi.org/10.1016/j.ydbio.2008.03.008.

Watanabe, S., Shioi, G., Furuta, Y., and Goshima, G. (2016). Intraspindle Microtubule Assembly Regulates Clustering of Microtubule-Organizing Centers during Early Mouse Development. Cell Rep. *15*, 54–60. https://doi.org/10.1016/j.celrep.2016.02.087.

White, M.D., Bissiere, S., Alvarez, Y.D., and Plachta, N. (2016). Mouse Embryo Compaction. Curr. Top. Dev. Biol. *120*, 235–258. https://doi.org/10.1016/bs.ctdb.2016.04.005.

Xie, H., Tranguch, S., Jia, X., Zhang, H., Das, S.K., Dey, S.K., Kuo, C.J., and Wang, H. (2008). Inactivation of nuclear Wnt-beta-catenin signaling limits blastocyst competency for implantation. Development *135*, 717–727. https://doi.org/10.1242/dev.015339.

Xu, W., Li, J., He, C., Wen, J., Ma, H., Rong, B., Diao, J., Wang, L., Wang, J., Wu, F., et al. (2021). METTL3 regulates heterochromatin in mouse embryonic stem cells. Nature *591*, 317–321. https://doi.org/10.1038/s41586-021-03210-1.

Ying, Q.L., Wray, J., Nichols, J., Batlle-Morera, L., Doble, B., Woodgett, J., Cohen, P., and Smith, A. (2008). The ground state of embryonic stem cell self-renewal. Nature *453*, 519–523. https://doi.org/10.1038/nature06968.

Zhou, Y., Zhou, B., Pache, L., Chang, M., Khodabakhshi, A.H., Tanaseichuk, O., Benner, C., and Chanda, S.K. (2019). Metascape provides a biologist-oriented resource for the analysis of systems-level datasets. Nat. Commun. *10*, 1523. https://doi.org/10.1038/s41467-019-09234-6.

Zhu, M., and Zernicka-Goetz, M. (2020a). Building an apical domain in the early mouse embryo: Lessons, challenges and perspectives. Curr. Opin. Cell Biol. *62*, 144–149. https://doi.org/10.1016/j.ceb.2019.11.005.

Zhu, M., and Zernicka-Goetz, M. (2020b). Principles of Self-Organization of the Mammalian Embryo. Cell *183*, 1467–1478. https://doi.org/10.1016/j.cell.2020.11.0034.